Graphical Abstract

From comparative connectomics to large-scale working memory modeling in macaque and marmoset

Loïc Magrou, Panagiota Theodoni, Amy F. T. Arnsten, Marcello G. P. Rosa, Xiao-Jing Wang

Highlights

From comparative connectomics to large-scale working memory modeling in macaque and marmoset

Loïc Magrou, Panagiota Theodoni, Amy F. T. Arnsten, Marcello G. P. Rosa, Xiao-Jing Wang

- Consensus mapping allows for directly comparing macaque and marmoset connectomes.
- Connectomes and spine counts constrain large-scale models of working memory.
- The marmoset model is susceptible to distraction, but not the macaque.
- Our results capture real life difference with regard to distraction.

From comparative connectomics to large-scale working memory modeling in macaque and marmoset

Loïc Magrou[a,b,c,j], Panagiota Theodoni[d,e,f,g,j], Amy F. T. Arnsten[h], Marcello G. P. Rosa[i], Xiao-Jing Wang[a,k,l]

[a] *Center for Neural Science, New York University, New York, 10003, NY, USA*
[b] *Department of Neurobiology, University of Chicago, Chicago, 60637, IL, USA*
[c] *Grossman Center for Quantitative Biology and Human Behavior, University of Chicago, Chicago, 60637, IL, USA*
[d] *Department of Philosophy, National and Kapodistrian University of Athens, Athens, 157 84, Greece*
[e] *Department of Psychology, Panteion University of Social and Political Sciences, Athens, 176 71, Greece*
[f] *College Year in Athens, Athens, 116 35, Greece*
[g] *Faculty of Pure and Applied Sciences, Nicosia, 2231, Cyprus*
[h] *Department of Neuroscience, Yale University School of Medicine, New Haven, 06510, CT, USA*
[i] *Department of Physiology and Neuroscience Program, Biomedicine Discovery Institute, Monash University, Clayton, 3168, VIC, Australia*
[j] *These authors contributed equally*
[k] *Lead contact*
[l] *Correspondence: xjwang@nyu.edu*

Abstract

Although macaques and marmosets are both primates of choice for studying the brain mechanisms of cognition, they differ in key aspects of anatomy and behavior. Interestingly, recent connectomic analysis revealed that strong top-down projections from the prefrontal cortex to the posterior parietal cortex, present in macaques and important for executive function, are absent in marmosets. Here, we propose a consensus mapping that bridges the two species' cortical atlases and allows for direct area-to-area comparison of their connectomes, which are then used to build comparative computational large-scale modeling of the frontoparietal circuit for working memory. We found that the macaque model exhibits resilience against distractors, a prerequisite for normal working memory function. By contrast, the marmoset model is sensitive to distractibility commonly observed behaviorally in this species. Surprisingly, this contrasting trend can be swapped by scaling intrafrontal

and frontoparietal connections. Finally, the relevance to primate ethology and evolution is discussed.

Keywords: Macaque, Marmoset, Consensus, Connectome, Anatomy, large-scale modeling, Working memory

1. Introduction

From Cuvier and Lamarck to Darwin and Wallace, comparative methods have historically been at the root of modern biology (Mayr, 1982). In neuroscience, recent advances of connectomics (Sporns et al., 2005; Hagmann, 2005), spanning from local (Harris and Mrsic-Flogel, 2013; Binzegger et al., 2009, 2004; Douglas et al., 1989) to multiregional (Theodoni et al., 2022; Majka et al., 2020; Dorkenwald et al., 2022; Scheffer et al., 2020; Harris et al., 2019; Gămănuţ et al., 2018; Markov et al., 2014a,b; Felleman and Van Essen, 1991) connectivity, offer a novel and quantitative approach to comparison between species. Comparative work on cortical connectivity has yielded important results in terms of graph theoretical (Theodoni et al., 2022; Horvát et al., 2016; Ercsey-Ravasz et al., 2013) and scaling properties of the brain (Magrou et al., 2024; Wang and Kennedy, 2016; Markov et al., 2013; Murre and Sturdy, 1995). However, whereas structural information is critical, it is often insufficient to predict dynamical behavior of a recurrent brain system, the understanding of which requires concomitant progress in physiological experiments and computational modeling (Wang, 2022).

In this context, Working Memory (WM), the brain's ability to internally maintain and manipulate information in the absence of sensory stimulation, has become a topic of focus, as its representation is distributed across multiple —- but not all — brain regions (Sreenivasan and D'Esposito, 2019; Christophel et al., 2017; Leavitt et al., 2017). In working memory dependent tasks, neurons in certain parts of the macaque cortex show robust, self-sustained, information-specific, mnemonic persistent activity (Goldman-Rakic, 1992; Fuster and Alexander, 1971; Wang, 2001, 2021). Experimental observations motivated connectome-based modeling of macaque monkey cortex for distributed working memory (Mejias and Wang, 2022; Froudist-Walsh et al., 2023). Consistent with experimental observations (Chafee and Goldman-Rakic, 1998), the reciprocal loop between posterior parietal cortex (PPC) and prefrontal cortex (PFC), making together the frontoparietal network, was found to play a major role in working memory. Furthermore,

a salient characteristic of normal WM is its resilience against distractors (Suzuki and Gottlieb, 2013; Olesen et al., 2007; Lorenc et al., 2021), which has been shown in modeling studies to critically depend on the PFC and its top-down influence onto the PPC in the macaque monkey cortex (Murray et al., 2017; Mejias and Wang, 2022; Froudist-Walsh et al., 2023).

Much less is known for the marmoset species, which is rapidly becoming another important animal model in our field (Prins et al., 2017; Mitchell and Leopold, 2015; Okano et al., 2012). Indeed, marmosets possesses many of the cognitive attributes of both macaques and humans, whilst being at the same time faster to breed and easier to handle in experiments. Additionally, and non trivially for the question at hand here, they were shown to possess the same frontoparietal network known to be the substrate of WM in macaques and humans (Reser et al., 2013), and have been recently shown exhibit sustained delay activity in the prefrontal cortex during WM tasks (Wong et al., 2023). Finally, the recent publication of the most complete retrograde tracer-based marmoset connectome available to date (Theodoni et al., 2022; Majka et al., 2020) allows for analysis and comparison with the macaque.

The in-depth investigation of the marmoset's WM capabilities is still at its early stage, but what seems to transpire from experimentalists is that, although they can perform such tasks, they are harder to train (Nakamura et al., 2018) and remain significantly more distractible than macaques (Joyce et al., 2024). Through this convergence of anatomical, functional and behavioral evidence, we find ourselves with the unique opportunity to push forward the comparative method into the realm of computational neuroscience. We can now apply the same model to both species, knowing that any behavioral difference that might emerge will be solely due to the differences in anatomy. Specifically, the differential distractibility could be captured with adequate modeling.

The present work tackles this important comparative question, with two main goals. We will first provide a common anatomical framework for the two species, which we have named "consensus mapping", whose purpose will be to reduce the macaque and the marmoset independent atlases to a common parcelation scheme where areal connectivity can be compared directly, and then convert all the available anatomical data to it, connectivity and spine count gradient alike. Second, we will constrain an otherwise identical model with those two sets of now one-to-one comparable anatomical data and investigate for commonalities and differences in the model's behavior.

2. Methods

2.1. Anatomical connectivity data

Despite the continuous progress occurring in the field of diffusion MRI and tractography based connectomics (Gajwani et al., 2023; Consagra et al., 2022), it nonetheless remains true that, where feasible, retrograde tract-tracing experiments still constitute the gold standard in cortical connectivity/mesoscale connectomics (Donahue et al., 2016). In the realm of primates, we are now uniquely suited to tackle cross-species comparison as extensive databases have been produced in both the macaque (Markov et al., 2014a; Froudist-Walsh et al., 2021, downloadable from core-nets.org), the historical model in primate neuroscience, and now the marmoset (Theodoni et al., 2022; Majka et al., 2020, downloadable from analytics.marmosetbrain.org), a smaller primate model that is easier to handle whilst retaining many primate features important to today's neuroscience.

Injections of retrograde tracers are carried out in multiple areas, designated as "target" areas, over multiple experiments. Each injection site is controlled so that the injection covers all 6 layers of the cortex, whilst not infringing on the white matter, so that the dye is not captured by fibers of passage. At the injection site, the dye is captured by axon terminals and is actively transported backward toward the soma of the cell, thus only labeling neurons that directly project onto the injection site (**Figure S1A**). These neurons are subsequently detectable through fluorescent microscopy. Tracers here employed are monosynaptic, meaning that they cannot continue their course beyond the one neuron that captured them into another neuron that shares a synapse with the back-labeled cell.

Labeled cells are counted and attributed to "source" areas according the species' parcelation atlas and their position with respect to granular layer 4 (*i.e.* infragranular for layer 5 and 6; supragranular for layers 2 and 3). From this data extraction are computed two basic connectivity metrics. The first one is the Fraction of Labeled Neurons (FLN; Falchier et al., 2002), defined as the number of labeled cells in a given area divided by the total number of labeled cells for the injection (*i.e.* in all cortical areas, excluding labeling in the injected area; **Figure S1B**), thus giving the relative weight of the connection. By doing so, all injections are normalized to 1, thus allowing comparison between injections. The second metric is the Supragranular Labeled Neuron (SLN; Barone et al., 2000), defined as the number of labeled cells in the supragranular compartment of an area divided by the total

number of labeled cells for that area (*i.e.* both infra and supragranular; **Figure S1B**). This metric allows us to quantify the feedforward/feedbackness of a connection, with values close to 0 being identified as feedback (FB) and values close to 1 as feedforward (FF). These SLNs can be used to produce a species specific cortical hierarchy (Markov et al., 2014b; Vezoli et al., 2021) that has been shown to correlate with cortical gradients of several biological measurements, such as areal spine counts (Mejias and Wang, 2022; Chaudhuri et al., 2015) or the recently discovered neurotransmitter receptor gradients (Froudist-Walsh et al., 2023). Over many injections, both metrics are usually displayed as matrices, with as many rows as there are areas in the relevant atlas (here macaque or marmoset), and as many columns as there is injections. Repeated injections are summed as if they where a single massive injection, which is consistent with standard practices when dealing with repeat injections, as in Markov et al. (2014a, 2011). In practice, what will be used throughout this paper is the square matrix (*i.e.* where source and target areas are the same) for each of those metrics, that is the edge-complete (*i.e.* all connections are known) graph of all commonly injected consensus areas.

2.2. Spine count gradient

The other anatomical constraint, besides connectivity, that is applied to the model is the gradient of spine count as investigated across several publications for both macaque (Elston et al., 2011, 2010, 2009; Elston and Rockland, 2002; Elston, 2001; Elston et al., 2001; Elston and Rosa, 1998b; Elston et al., 1999b; Elston and Rosa, 1998a, 1997) and marmoset (Oga et al., 2013; Sasaki et al., 2015; Elston et al., 2001, 1999a). Spine counts, as captured by the total number of spine on the basal dendrites of layer 2/3 pyramidal cells, have been shown in macaques to vary across areas by more than ten-fold from 600 in V1 more than 8000 in premotor areas. Further, Nimchinsky et al. (2002) showed that approximately 90% of excitatory synapses on neocortical pyramidal cells are on dendritic spines, thus making a strong argument that a greater amount of spines results in a greater excitability. Elston (2007) in turn suggested that spine count differences are likely to impact local summation of postsynaptic potentials. Because of this, spine counts can be used as a proxy to the self connectivity of a population.

Additionally, it is a non trivial discovery that these spine count values correlate positively with the SLN-based cortical hierarchy for both macaque and marmoset (Mejias and Wang, 2022; Theodoni et al., 2022; Chaudhuri

et al., 2015), computed from retrograde tracer connectivity where the hierarchy is statistically inferred through a beta-binomial GLM applied to the SLN values (Vezoli et al., 2021; Markov et al., 2014b). This conception of hierarchy is itself rooted in the anatomical understanding of FB and FF (Felleman and Van Essen, 1991; Van Essen and Maunsell, 1983; Rockland and Pandya, 1979). The very fact of this correlation means that the hierarchy captures an important aspect of cortical areal differences, which can be used to complete the data where missing. All spine count values and their corresponding bibliographical references are given in **Table S1 and S2**, along with their hierarchical index.

2.3. Consensus mapping: Atlas

One of the key requirements of a formal comparative analysis of nervous systems is a step aimed at mapping the anatomical knowledge available for one species into registration with that available for the other. In the present study, this requirement translated into identifying homologous parcels of cerebral cortex in the marmoset and macaque, so the patterns of connectivity could be directly related within a same spatial reference frame. This process was, in practice, limited by issues related to the use of different nomenclatures by different laboratories, data availability (*e.g.* the areas explored with tracer injections may not be the same in the two species), and the likelihood of genuine biological differences. To circumvent such issues, we created a consensus map that describes the subdivision of the cortex of the two species in a manner that results in identification of the same number of homologous parcels (areas, or groups of areas) for which the results of tracer injections were available (**Figure 1, Table S3**).

This consensus mapping provides a way to directly relate the cortical areas proposed by Paxinos et al. (2012) in the marmoset, which recognizes 116 histologically distinct areas, and those proposed by Markov et al. (2014a) in the macaque, which recognizes 91 areas. These atlases were chosen because they were used as the basis for describing the most comprehensive cellular-level connectomic datasets available (Theodoni et al., 2022; Majka et al., 2020; Froudist-Walsh et al., 2021; Markov et al., 2014a,b). Alignment of the two parcelations was guided by several criteria, which included location in the brain and relative to other areas, histological structure, and, where available, functional data and pattern of connectivity.

In the simplest case, single areas could be directly identified in the two species using available histological and functional criteria. For example, the

majority of the areas of the visual and premotor cortex could be identified with a high degree of certainty based on previous anatomical and functional studies (Solomon and Rosa, 2014; Bakola et al., 2015). In other cases, one area in one species was related to 2 or more areas in the other. For example, the marmoset caudal somatosensory cortex is not clearly differentiated into areas 1 and 2, as in the macaque, and appears instead the single area A1-2. Conversely, whereas marmoset area 3 is subdivided into A3a and A3b, the macaque atlas only provides a single subdivision called area 3. More complex mappings were required, leading to larger parcels. For example, in the macaque medial temporal lobe, area TH/TF was equated to five areas in the marmoset cortex: TF, TFO, TH, TL and TLO. At the end of this process, we are left with an consensus atlas of 75 areas. Let it here be noted that the subiculum ("SUBI" in **Figure 1**), entryway to the hippocampus proper and part of the hippocampal formation, is not part of the marmoset original parcelation, and therefore absent from the consensus one as well, effectively bringing down the consensus to 74 areas, since keeping the subiculum in the macaque is non consensual. Nonetheless, it was kept for completeness sake, and is not involved in the simulations reported here. The complete table of consensus equivalence across the two species is available in **Table S3**.

2.4. Consensus mapping: Computing connectivity

The consensus atlas now set, the connectivity of the two independent dataset must be converted to this new atlas of 74 common consensus areas, before they can be fully compared and used in a large-scale model. To do so, FLN, SLN and spine count values have to be combined so as to fit the new parcelation. As the consensus is essentially merging areas and area subdivisions together in either species to converge on homolog parcelation schemes, the connectivities of both species should reflect this by summing together source areas at the level of neuron counts. In other words, all the relevant connectivity transformations happen in the count matrices, created from the downloadable material for both species (see section 2.1). It must be stressed that to do so, one needs separated neuron count matrices for infragranular and supragranular numbers for both species, and that any operation needs to happen in the same fashion in both infra and supragranular matrices for each species.

For a given injection, two source areas (*i.e.* two rows in the count matrix) that need to be merged will see their respective counts of neurons summed together as a single area. Additionally, two target areas (*i.e.* two columns

in the count matrix) will also be summed together, as if it were a large unique injection. The decision to sum, as opposed to average them together, follows the same logic as with the repeat injections explained above (Markov et al., 2014a, 2011). It stems from the fact that computing FLNs and SLNs are linear transformations that both involve dividing by the cumulated sum across injections. Additionally, averages tend to create non integer quantities for counts, where summing does not.

Once the new count matrices are ready and conform to the consensus parcelation, the macaque original matrices of 40×91 have become 35×74 matrices under consensus. Similarly, the marmoset ones have changed from 55×116 to 45×74. Complete consensus FLN and SLN matrices can be examined in **Figure S2 and S3** and full consensus data is available in **Table S5**. Of the 35 and 40 consensus injected areas for the macaque and the marmoset respectively, 29 are commonly injected in both species. Common consensus square FLN and SLN matrices of size 29×29 (**Figure 2 and S4**) are then extracted and, in the case of FLN, columns are renormalized to sum to 1.

2.5. Consensus mapping: Spine Count gradient

Merging spine counts to follow the consensus parcelation leads to two potential cases: either merging 2 areas (or more) that all have spine counts attributed to them prior to consensus, or merging 1 area that has a spine count with another area that does not. Through sheer happenstance, the first case never did present itself in either species, due in part to the fact that spine counts have been measured in the context of broader areas (*i.e.* area 46 or TE, which are larger than the currently used parcelation), and in part because far from all pre-consensus areas have been tested for spine counts. When the second case presented itself, the most parsimonious position was to assume homogeneity, and therefore attribute the spine count value of the first area to the resulting consensus area. This more parsimonious approach is further validated because spine counts are computed for an average neuron in each area.

In the case of consensus areas for which no spine count data was available prior to consensus, then the SLN-based hierarchy was used, itself computed from the consensus SLN matrices, as explained in section 2.2 and 2.8, following the methods from Vezoli et al. (2021) and Markov et al. (2014b).

2.6. Consensus mapping: 11×11 matrices

In order to study the particularities of the WM system proper, we expended the 2-compartment model of Murray et al. (2017), which modeled PPC and DLPFC with each with a single Wong-&-Wang, into an 11 area model, where PPC and DLPFC are now 6 and 5 areas, respectively. Doing so therefore encompasses all available consensus data regarding the parietofrontal network, known to be the substrate of WM (Goldman-Rakic, 1992). These 11×11 matrices can be seen in **Figure 4B** and consist of 6 PPC and 5 DLPFC consensus areas. The corresponding spine count values were taken from the consensus spine count gradient described above in section 2.5.

2.7. Computational model: local circuit

Conceptually, the system built here should be thought about as a network of Wong-&-Wang models (Mejias and Wang, 2022; Wong and Wang, 2006), each corresponding to a particular cortical area, and whose connectivity to other areas (*i.e.* other Wong-&-Wangs) are structured and constrained by the retrograde tracer connectivities described above (**Figure 3A**).

The local system, which belongs to the category of mean-field models, possesses in our case three explicit variables r_A, r_B and r_C, describing the temporal evolution of the firing rates of three neural populations: two excitatory (populations A and B) and one inhibitory (population C). The equation of the firing rate for each population is as follows:

$$\tau_r \frac{dr_i}{dt} = -r_i + \Phi_i(I_i) \tag{1}$$

Here, and in all future equations, all parameter values are taken from Mejias and Wang (2022), except G and ρ. The index i can be A, B or C, depending on the population. $\tau_r = 2$ ms and $\Phi_i(I_i)$ is a transfer function that converts the total current I of a population into a firing rate, according to the following equations (Abbott and Chance, 2005):

$$\Phi_{A,B}(I) = \frac{aI - b}{1 - exp(-d(aI - b))} \tag{2}$$

$$\Phi_C(I) = \left[\frac{1}{g_I}(c_1 I - c_0) + r_0\right]_+ \tag{3}$$

with $a = 135$ Hz/nA, $b = 54$ Hz, and coefficient $d = 0.308$ for equation (2); and $g_I = 4$, $c_1 = 615$ Hz/nA, $c_0 = 177$ Hz and $r_0 = 5.5$ Hz for equation (3). The index "+" in $[expr]_+$ indicates a rectification where all negative values are set to 0.

Given that Φ_i evolves as a function of I_i, let us define next the current equations for each population:

$$I_A = J_s S_A + J_c S_B + J_{EI} S_C + I_{0A} + I_{net,A} + x_A(t) \tag{4}$$
$$I_B = J_c S_A + J_s S_B + J_{EI} S_C + I_{0B} + I_{net,B} + x_B(t) \tag{5}$$
$$I_C = J_{IE} S_A + J_{IE} S_B + J_{II} S_C + I_{0C} + I_{net,C} + x_C(t) \tag{6}$$

Starting with the fixed parameters for this set of equations, the cross-coupling parameter J_c has a value of 0.0107 nA and encapsulates how the two excitatory populations A and B cross-activate each other. J_{EI} is the coupling parameter regulating the input from inhibitory population C into excitatory populations A and B. Being inhibitory, the term $J_{EI} S_C$ must be negative, so J_{EI} is set at -0.31 nA. J_{II}, population C inhibitory input onto itself, is also negative at -0.12 nA. Background current parameters I_{0A} and I_{0B} are identical and set at 0.3294 nA, I_{0C} is set at 0.26 nA.

Although fixed, the self-coupling parameter J_s and the excitatory-to-inhibitory coupling parameter J_{IE} are different for each area depending on the spine count gradient (see section 2.2) and will be explained in a dedicated section down below (section 2.8). Similarly, the $I_{net,i}$ terms for each populations, which encapsulates the role of the inter-areal anatomical connectivity (section 2.1), requires its own dedicated explanations further down (section 2.9).

The variables collectively designated as S_i are described by the conductance equations below, and truly govern the local system:

$$\frac{dS_A}{dt} = -\frac{S_A}{\tau_N} + \gamma_E (1 - S_A)\, r_A \tag{7}$$
$$\frac{dS_B}{dt} = -\frac{S_B}{\tau_N} + \gamma_E (1 - S_B)\, r_B \tag{8}$$
$$\frac{dS_C}{dt} = -\frac{S_C}{\tau_G} + \gamma_I\, r_C \tag{9}$$

In these, S_i are the conductances for each population; the τ_N (NMDA) and τ_G (GABA) time constants are set at 60 and 5 ms respectively; and γ_E and

γ_I, set at 1.282 and 2, are dimensionless saturation factors for the excitatory and inhibitory populations, respectively again. Finally, r_i is the firing rate of each population from equation (1).

The last term in the current equations (4-6), $x_i(t)$, signifies an Ornstein-Uhlenbeck process, which introduces some level of stochasticity, and can be construed as random noise intrinsic to the system. It is defined be the following equation:

$$\tau_{noise}\frac{dx_i}{dt} = -x_i + \sqrt{\tau_{noise}}\ \sigma_i\ \xi_i \tag{10}$$

where τ_{noise} is the time constant for the process set at 2 ms, σ_i is the noise strength set at 0.005 nA for populations A and B, at 0 for population C. The last term ξ_i is the Gaussian white noise, on which σ_i is applied.

Finally, still in equations (4-6), an implicit term μ can be added to introduce sensory stimulations into the system, in which case $\mu = 0.3$ nA for a duration of 500 ms. **Figure 4D** shows the schematic progression of the task modeled in this study, with the cue and the distractor stages being where μ is non zero for one of the populations.

2.8. Computational model: Spine count gradient as synaptic strength

What makes large-scale models increasingly important as neuroscience progresses is their ability to incorporate differences between cortical areas, where they would otherwise be construed — and modeled — as rigorously identical units. Here, we use a brain wide gradient of spine count to uniquely constrain our system, whereby each area is characterized by a spine count value, as exposed in section 2.2, which is used to compute an area-specific self-coupling parameter J_s through the following equation:

$$J_s(a) = J_{min} + (J_{max} - J_{min})\ \frac{\tilde{h}_a}{\tilde{h}_{max}} \tag{11}$$

where a is a consensus area; J_{min} is the minimal synaptic strength set at 0.21 nA; and J_{max} is the maximal value synaptic strength can take, set at 0.42 nA, effectively bounding J_s between those to values. $\tilde{h}_a/\tilde{h}_{max}$ is meant to represent the normalized spine count gradient, completed by SLN-based hierarchical estimates $\hat{h}_a$ where necessary (see **Table S1**). This effectively produces a gradient of J_s values, spanning from J_{min} to J_{max}. J_{max} being inferior to bifurcation threshold J^* ensures that no single area taken alone is able to achieve multistability (**Figure 4C**).

From J_s is computed J_{IE} with the subsequent equation:

$$J_{IE}(a) = \frac{1}{2J_{EI}\zeta}(J_0 - J_s(a) - J_c) \tag{12}$$

where a is again an area; J_c and J_{EI} are the same parameters as in equations (4-6), set at 0.0107 and -0.31 nA respectively. Parameter ζ is fixed on parameters previously spelled out:

$$\zeta = \frac{\tau_G \ \gamma_I \ c_1}{g_I - J_{II} \ \tau_G \ \gamma_I \ c_1} \tag{13}$$

with τ_G and γ_I from equation (9); c_1 and g_I from equation (3); and J_{II} from equation (6). The explanation for the precise definition of ζ can be found in the methods of Mejias and Wang (2022). Briefly, the baseline activity level of each local Wong-&-Wang circuit is by default dependent on J_s, and areas with high values could exhibit spontaneous persistent activity. They could in principle even go beyond physiologically realistic limits if left unbounded. We control this by imposing on the system that all areas have the same baseline, regardless of their specific J_s value. We allowed three simplifying assumptions: The system is symmetrical with respect to populations A and B (at baseline, the only input the background current, and $I_{0A} = I_{0B}$), noise is negligible, and population C has significantly faster dynamics, as they are mediated by GABA. After simplification, equation (12) and (13) are deduced, with J_0 being set at 0.2112 nA. The linear relationship described in equations (11) and (12) ensures that the baseline activity is the same for all areas in the network. Note that deviations from this linear relationship would simply lead to different areas having slightly different spontaneous activity levels, but it does not substantially affect our main results.

Because J_{IE} needs to always be non negative, equation (12) imposes a lower bound to the values J_s can take in equation (11) at 0.205 nA. On the other side of its range, a J_s that would be higher than the bifurcation point of the system (0.4655 nA for an isolated Wong-&-Wang parametrized as described so far) would grant multistability to the system. Therefore, setting J_{max} below that bifurcation threshold ensures that all areas are monostable when taken in isolation. In other worlds, each individual area cannot on its own display sustained activity, even after a stimulation, and any persistent non baseline firing rate is strictly an effect multi-areal system as a whole. Here, as described above, setting J_{min} and J_{max} at 0.21 and 0.42 nA respectively ensures that our system displays distributed working memory as a non linear effect of associating monostable areas together.

2.9. Computational model: Inter-areal connectivity

Going back to equations (4-6), the term $I_{net,i}$ still requires explanations. This term designates the current that, for each population in each area, comes from the rest of the network outside the area in question. Said differently, it is the global input current to each area, and is defined as such:

$$I^x_{net,A} = G \sum_y W^{xy}\ SLN^{xy}\ S^y_A \tag{14}$$

$$I^x_{net,B} = G \sum_y W^{xy}\ SLN^{xy}\ S^y_B \tag{15}$$

$$I^x_{net,C} = \frac{G}{Z} \sum_y W^{xy}\ (1 - SLN^{xy})\ (S^y_A + S^y_B) \tag{16}$$

In these, indices x and y respectively represent rows and columns of matrices W^{xy} and SLN^{xy}, where each column is a target area (*i.e.* injection site) and each row is a source area. Additionally, y the y^{th} element in column vector S^y_i. The summation over y applies over the expression $W^{xy}\ SLN^{xy}\ S^y_i$ (or the population C equivalent), which is the pairwise (*i.e.* Hadamard) product of matrices W, SLN and column vector S_i. The output of said summation is the row vector $I^x_{net,i}$, where x is the x^{th} element in the vector.

G stands for the global coupling parameter, which tunes up or down the importance of the input from the network to a given area. The exact value of G is different for the two species (see Results: Standard Behavior) and are set at 0.98 and 0.85 for macaque and marmoset respectively, for all simulations. Z is a scalar that controls the balance between excitatory and inhibitory inter-areal connections. $Z = 1$ would mean that long-range excitatory and inhibitory projections are of equal strength. In our particular case, we needed to enforce the following condition: if excitatory populations A and B are both active at the same time and at the same level in a given area, then their net effect on other areas in the network should be 0. Given this imperative, parameter Z can be deduced as follows:

$$Z = \frac{2c_1\ \tau_G\ \gamma_I\ J_{EI}}{c_1\ \tau_G\ \gamma_I\ J_{II} - g_I} \tag{17}$$

with c_1 and g_I from equation (3); τ_G and γ_I from equation (9); J_{EI} and J_{II} from equations (4-6).

Back to equations (14 to 16), W^{xy} is the weight matrix, which we get to through the following sequence of transformations: First we define the

matrix U as the non linear rescaling of matrix FLN (see section 2.1):

$$U^{xy} = k_1(FLN^{xy})^{k_2} \tag{18}$$

where k_1 and k_2 are rescaling factors of value 1.2 and 0.3 respectively. The rescaling described by equation (18) is done so that the range of FLN values, which spans 5 to 6 orders of magnitude, is better suited to a firing rate model.

We then renormalize U by column to obtain V:

$$V^{xy} = \frac{U^{xy}}{\sum_y U^{xy}} \tag{19}$$

Importantly, this renormalization step, named as such to differentiate it from the original normalization that produces FLNs, is to be performed only once, on the edge-complete 29×29 matrix. The 11×11 connectivity matrix of parietal and prefrontal areas is not renormalized again, as it is considered a subpart of a larger network, not its own independent system.

Finally, to obtain our true weight matrix W, the spine count gradient is introduced to the inter-areal connectivity so that global and local circuitry be of the same trend, like so:

$$W^{xy} = \frac{J(s)}{J_{max}} V^{xy} \tag{20}$$

Going back once more to the $I_{net,i}$ equations (14-16), the SLN term indicates the square matrix of SLN values, already described in 2.1. As SLN values evolves between 0 and 1, with 0 meaning FB and 1 as FF, pairwise multiplication of the SLN and the W matrices gradually filters out FBs as a function of the SLN value. If it is a reasonable assumptions that FFs should be excitatory, as it facilitates signal propagation to the entire system, having FB do the same would lead to excitatory reverberation and all areas being indiscriminately activated as well as having similar firing rates during working memory delay, as shown by Mejias and Wang (2022). In the same paper, the authors introduce the notion of Counterstream Inhibitory Bias (CIB), by which the weight matrix W is, for the inhibitory population C of each area, not pairwise multiplied by SLN but by $(1 - SLN)$, thus filtering out FF connections, not FB ones. By doing so, the model effectively takes on the assumption that FBs connect to inhibitory neurons which, if it is very much consistent with the known FB modulatory effects (Tsushima et al., 2006; Hupé et al., 1998; Girard and Bullier, 1989), the existence of such

FB-to-inhibitory-cell connections still remains to be proven at the cellular level. That being said, applying the CIB to a distributed working memory model does yield a pattern of sustained activity during working memory that is remarkably close to known electrophysiological data (Mejias and Wang, 2022), thus making the CIB a fascinating as well as credible prediction to be tested by experimentalists.

Finally, all parameters of the model are listed in **Table S4**.

3. Results

3.1. Connectome data, hierarchy, and spine counts

The 29×29 square consensus connectivity matrices (**Figure 2**), comprise a total of 794 and 809 connections for the macaque and the marmoset respectively, over a total of $29 \times 28 = 812$ possible connections (self connections are ignored), leading to respective graph densities of 0.68 and 0.72. For the macaque, the distribution of $\log_{10}$ FLN (*i.e.* connection weights) is best approximated by a normal distribution, with a mean of -2.60, which is slightly lower than that of the marmoset at -2.28, which is consistent with previous results from Theodoni et al. (2022) in spite of modifications produced by the consensus (**Figure 3A**). Also consistent with previous work, if the macaque spans the usual 6 orders of magnitude, as described elsewhere (Markov et al., 2014a, 2011), the marmoset spans only 5 of those orders (Theodoni et al., 2022; Majka et al., 2020). Correlation between macaque and marmoset $\log_{10}$ FLN data is 0.59. Notably, The marmoset lacks some of the top-down connections from DLPFC to PPC that the macaque has, notably from area 46d_9/46d to LIP, which is a major contributor to spatial WM in the macaque. Conversely, the macaque appears to be missing some — albeit weak — connections from area 10 to medial parietal and posterior visual areas, suggesting that A10 in marmoset may retain some features of the more posterior prefrontal areas, such as the frontal eye field (A8aD_A8aV) (**Figure 2B**).

Differences are greater in terms of SLN (**Figure 3B**), where correlation between the two species is weak ($r = 0.32$) and where the macaque average ($\mu = 0.47$) is lower than that of marmoset ($\mu = 0.59$), meaning that macaque connections tend to be, on average, more FB (**Figure S5**), consistently with the non consensus original data (Theodoni et al., 2022; Majka et al., 2020). **Figure 3C** shows the difference in SLN-based hierarchical estimates (Vezoli et al., 2021; Markov et al., 2014b) for the two species, with areas ordered

on the macaque hierarchy. Marmoset consensus areas A3a_A3b (primary somatosensory for touch and proprioception), A4ab_A4c (primary motor or M1) and, to a lesser extent marmoset area A1-2 (primary somatosensory for texture, size and shape) and PE_PEC (somatosensory dedicated to forelimb digits and joints), which also receives direct somatosensory thalamic inputs (for a detailed review of primate S1, see Delhaye et al., 2018), have a higher hierarchical value than their macaque counterparts (macaque areas 3, F1 1_2 and 5 respectively). This, again, is consistent with the pre-consensual data (Theodoni et al., 2022). In other words, somatosensory and primary motor modalities are higher in the global cortical hierarchy in the marmoset than they are in the macaque. At the top of the marmoset hierarchy is consensus area A6Va_A6vb (macaque consensus area 44_F5, motor oro-facial homolog to Wernicke in humans).

Conversely, marmoset prefrontal areas A45, A9, A47 (macaque area 12) and A10 have lower hierarchical values than their macaque counterparts. Other interesting differences also occur in the visual system, such as marmoset areas V4 , OPt and MIP (V4, DP and MIP in the macaque), which also display higher hierarchical estimates. Thus, a general picture seems to emerge, whereby sensory-motor areas are tendentially higher in the hierarchy for the marmoset, when more associative areas tend to be higher in macaques.

Spine counts have been shown elsewhere to correlate positively with SLN-based hierarchy in macaques (Mejias and Wang, 2022; Chaudhuri et al., 2015). Here, we show that the marmoset species also displays a correlation of spine count with hierarchy, albeit different in slope (**Figure 3D**). This is yet again consistent with pre-consensus data (Theodoni et al., 2022), thus further validating that the consensus process conserves properties well. In the current consensus data, the maximum spine count density value is just short of 5000, whereas macaque maximal values go beyond 8000. This may be due to lack of data, but available data for the homolog areas in both species suggests a genuine difference in spine counts (see marmoset areas A9, A10, TEO and TE3, and macaque counterparts 9, 10, TEO_TEOm and TEa/ma_TEa/mp_TEpd.

3.2. Standard behavior of the 11×11 consensus area model

Because the 11×11 model does not contain primary sensory areas, both cues (always in excitatory population A) and distractors (always in excitatory population B; **Figure 4D**) are sent to all parietal areas, so as to reflect the distributed input those areas should normally receive from the early visual

system. Additionally, sending the cue to a single parietal area fails to create persistent and distributed activity in the system, and only a combination of 4 to 5 parietal areas (depending on elected areas) achieves the goal of distributed sustained activity. Cues are always sent at 1 s into the simulation, and distractors at 4.5 s. Finally, the system is symmetric in the sense that population A and B stable points are identical in terms of firing rate values, as already established in Mejias and Wang (2022).

All free parameters of this model are fixed at the same values for both species except for global coupling strength parameter G, which requires specific parametrization for each species to meet certain basic behavioral criteria. These basic criteria are the following: 1) being able to produce distributed and sustained activity; and 2) not to produce spontaneous sustained activity if not solicited by a cue in either excitatory population.

We determined the valid range of G values by doing a systematic parameter search with gradual incrementation of step size 0.01 for both species, using 10 s simulations over 20 different random seeds (**Figure 5A**). Valid range of value go from 0.80 to 1.16 in the macaque, versus 0.57 to 1.13 in the marmoset (averaged over the 20 seeds for both species). Final values of G were chosen as the mid point of the resilient range for the macaque and the distractible range for the marmoset, at 0.98 and 0.85 respectively (**Figure 5A**). Specific to the macaque system is the existence of a regime of partially resilient behavior (from 0.45 to 0.80), where prefrontal areas show persistent activity but parietal areas fail to do so (**Figure 5B**, complete set in **Figure S6A**). Additionally, there exists a small, not robust, window of low G values (between 0.50 and 0.57) that produces a resilient marmoset (**Figure 5C**, complete set in **Figure S6B**).

With G now fixed, both species in the 11×11 model display similar behavior in response to the cue, in that both achieve distributed sustained activity throughout the system prior to the onset of the distractor (**Figure 6**, purple trace). Note the very low rate of areas DP and 8l_8m_8r in the macaque compared to their marmoset equivalents, OPt and A8aD_A8aV. A major difference in behavior arises after sending the distractor in excitatory population B. At that point, the macaque shows a resilience to distraction (**Figure 6A**, purple trace) when the marmoset's population B takes over (**Figure 6B**, green trace). Beyond the susceptibility to distraction shown in **Figure 6**, macaque area DP and consensus area 8l_8m_8r (*i.e.* the FEF), fail to achieve strong activity, contrary to their marmoset counterparts OPt and A8aD_A8aV (marmoset FEF). This difference is not dependent on

parametrization.

The activity of macaque DP and FEF is not exactly 0, since DP averages around 1.8 Hz and FEF around 1.3. Such a reduced, yet non-zero activity is indication of reduced input from the rest of the network. Looking back at **Figure 3B**, the average of (non logged) FLN input from the parietal is ~ 0.008 for the macaque and ~ 0.014 for the marmoset. Cumulatively, the macaque FEF receives from parietal areas less than 0.6 times what the marmoset FEF receives from the same areas (~ 0.049 vs ~ 0.082). In comparison, the intrafrontal input to the FEF (*i.e.* from the other prefrontal areas) is greater in the macaque than in marmoset, with non-log averages of ~ 0.066 and ~ 0.015 respectively. The cumulative sums of FLNs for each are ~ 0.263 and ~ 0.059, that is a 4.4 times larger input for the macaque.

A similar observation can be made for DP/OPt: the connection average FLN from other parietal areas is ~ 0.061 for the macaque and ~ 0.153 for the marmoset, for a cumulative input of ~ 0.183 vs. ~ 0.765, about 4.2 stronger in the marmoset. comparatively, input from the prefrontal areas to DP/OPt are very weak, averaging ~ 0.0017 for the macaque and ~ 0.0006 for the marmoset, with a cumulative sum of ~ 0.0067 and ~ 0.0026 (~ 2.5 higher for the macaque, but still a very weak connection).

Additionally, SLNs are also at play: FEF and DP in the macaque average at ~ 0.360 and ~ 0.428 respectively, vs. ~ 0.698 and ~ 0.669 for the marmoset. This means that, all things being otherwise equal, FEF and DP are non negligibly more FB in the macaque than they are in the marmoset, which is not the case for the any other area, with the exception of 7A/PFG_PG.

In summary, the macaque FEF indeed receives less cumulative parietal inputs and more prefrontal inputs than it does in the marmoset, as is the case for macaque area DP compared to its marmoset homolog OPt. Adding to this the fact that connections to both macaque FEF and DP are more FB than in the marmoset, and therefore more inhibitory *via* the CIB, we see that the anatomy easily explains the dynamical difference between the two species.

Finally, the next logical step of running a full 29×29 version of this model failed to yield the same species difference (**Figure S7**). At that scale, the cue, sent to V1 of both species, propagates to all areas and a later distraction even in the marmoset is unable to take over the system.

3.3. Bridging the gap between species

In order to understand what makes macaque and marmoset different in their distractibility, we investigated how we could make the macaque model susceptible to distraction and, vice-versa, force the marmoset to be resilient to distractors. Swapping around the specifically macaque connections to the marmoset and vice-versa failed to yield the expected result (**Figure S8**). We therefore elected to divide the 11×11 connectivity matrices of both species into 4 quadrants, and attributed to each a specific multiplicative parameter, from ρ_1 to ρ_4 (**Figure 7A**). The parameter space of ρ_1 vs. ρ_2 is showed in **Figure 7B**. Conversion can be achieved in the macaque by reducing ρ_1 to any value below 0.6 (**Figure 7A**), thus effectively tuning down the intra-frontal connectivity. The consequence of this is to shift the system to a part of the parameter space where distraction can occur (**Figure 7B**, left panel, leftward arrow). Sensitivity to distraction in the macaque can be observed in example areas DP, LIP, 8l_8m_8r (FEF) and 46d_9/46d **Figure 7C**. LIP and 46d_9/46d are shown as good prototypical areas for parietal and prefrontal regions, respectively. DP and the FEF are shown because of their lack of activity in the macaque, as already visible in **Figure 6** (complete set in **Figure S9A**).

As can be seen in **Figure 7B**, the macaque possesses what appears to be another distracted territory for very high values of ρ_1, with gradual transition roughly centered around 1.8. However, this part of the parameter space is in fact unstable as the outcome behavior depends on the random seed used in any particular simulation. This is indicative of a parameter going beyond its "physiological", or at least realistic, limits. At these levels, any random fluctuation is amplified by a factor of close to 2 in the prefrontal areas. Helped by a higher firing rate baseline also due to the higher ρ_1 value, this leads to an easy propagation to rest of the network. Due to their unrealistic nature, these will not be discussed further in what follows.

A marmoset resilient to distraction can similarly also be achieved by giving ρ_1 and ρ_2 the value of at least 1.4 each (**Figure 7C**), which effectively displaces the system to a part of the parameter space that grants it resilience (**Figure 7B**, right panel, right-upward arrow), with example areas showcasing the behavior in **Figure 7C** (Complete set in **Figure S9B**). A mixed behavior regime exists in the marmoset's ρ_1-ρ_2 plane, which is characterized by partial activations in the system (**Figure S9C**).

As a side note, similar parameter spaces can be achieved with ρ_3 and ρ_4 that also show different domains of resilience and susceptibility, which are

topologically similar to the ones of ρ_1 and ρ_2 (**Figure S10C**). There, the macaque becomes sensitive to distraction as one increases ρ_4, and the marmoset becomes resilient by reducing both ρ_3 and ρ_4. For practical purposes, the focus will bear on ρ_1 and ρ_2 in what follows.

The next logical step was then to try and understand the transition from one regime to the other. To do so, we performed simulations at incremental steps in the ρ_1 parameter space dimension, across the border that separates the two regime, and looked at the conductance S_A-S_B space (*i.e.* Excitatory populations A and B's S variable) for the system's trajectories, using each time 10 different random seeds. For the macaque, ρ_2 was fixed at a value of 1, and $\rho_1$varying from 0.75 to 0.55 (*i.e.* from resilient to distractible) with steps of 0.01 (**Figure 8A**, ρ_1-ρ_2 panel). **Figure 8A** displays the state of the macaque S_A-S_B phase portrait (rotated by $\pi/4$) for increasing values of ρ_1. At $\rho_1 = 0.72$ (first panel on the left, full progression visible in **Video S1**), the macaque displays its standard behavior. The at-rest stable fixed point (black dot) is reached within a small number of time steps (black trajectory originating from coordinate (0,0)) and the system will stay there until the cue is delivered. Said cue can be sent to either population A (purple trajectory) or population B (green trajectory). In either case, the system will reach the stable fixed point specific to the population that was cued (purple point for population A, green point for B), after a quick overshoot. At that point, a distractor can be injected in the opposite population. When doing so, the system's trajectory shoots inward for the duration of the pulse (trajectories yellow and red), only to come back the same stable fixed point they were at before distraction.

Trajectories will become increasingly tempted by the other side as ρ_1 decreases. Transition into to the distractible regime of behavior for the macaque occurs over a very narrow band of ρ_1 values, contained between 0.64 and 0.63, where independent random seeds show radically different trajectories, some showing resilience and returning to their fixed point of origin, and others showing susceptibility and ending their course on the opposite stable fixed point. From $\rho_1 = 0.62$ downward, the system has fully transitioned to being distractible and all seeds display similar behavior once again, this time to be diverted to the opposite fixed point.

Looking now at the marmoset, we followed an identical procedure, only fixating ρ_2 at a value of 1.5 so as to avoid going through the mixed regime of behavior (**Figure 8B**, ρ_1-ρ_2 panel). ρ_1 was there set to vary this time from 0.975 to 1.175, again with steps size of 0.01. Qualitatively, the behavior

is reversed from the macaque, as the marmoset is by default sensitive to distraction. At $\rho_1 = 0.985$, well before the transition happens, trajectories are quite analog with those of the distractible macaque. As ρ_1 progresses toward the threshold of behavioral shift, random seed trajectories remain well grouped together, and will remain so during and after the transition, which is an interesting qualitative difference with the macaque, arguing for a qualitatively different high dimensional landscape, as they might in fact be fanning out in a different plane. The transition itself even shorter than in the macaque, as all seeds have transitioned at $\rho_1 = 1.075$ to a fully resilient marmoset. Interestingly, these distractor-based trajectories still show a small detour along their former distractor sensitive path before turning around toward their newly found target. The last of this can be seen at $\rho_1 = 1.105$ (**Video S2**).

4. Discussion

4.1. Relevance of consensus mapping

The consensus mapping that we have exposed and successfully used here offers the unique opportunity to directly compare the mesoscale connectomes of two species of primates. Allowed by the extensive anatomical analogies that exist between primates, the consensus mapping is largely based on the merging of subareas together to recover coarser-grained areas. This comes at the price of loosing some of the spatial granularity for either species. Nonetheless, as we have seen with **Figure 3 and S5**, the consensus process conserves the basic statistics, FB and FF distributions, graph densities and spine count to hierarchy relationship (Theodoni et al., 2022; Ercsey-Ravasz et al., 2013; Markov et al., 2013) of each species pre-consensus. Therefore, the mapping is stable enough to be meaningful for the modeling depicted in this study. Future anatomical investigations of these two species will continue to improve the overlap of injected areas, and should prove important for future comparative work in primate anatomy.

4.2. Parametrization of the marmoset

The most crucial finding of this study is the fact that the macaque and marmoset models, which are identical if not for their anatomical data, capture an important and real cognitive difference between the actual species in their resilience to distraction. But for the readers to assess carefully the

validity if this result, some aspects of the modeling need to be further discussed. The first of them is how the global coupling parameter G (**Figure 5A**) value was chosen. In the macaque, the parametrization is fairly straightforward, given that there is only one bracket of values that produces a fully distributed activity without running the risk of spontaneous activity, with no possible values offering the possibility of a distractible system. The marmoset on the other hand, although its largest window of viable activity is indeed the distractible one, does have a valid, if narrow and less robust, window of resilient behavior. Therefore, purposefully choosing a distractible G value to then claim that our model captures differential distractibility may at first glance look like a self-realizing prophecy. However, that would be missing the point, which is that the macaque possesses no distractible G values when the marmoset is mostly distractible for the same range of values, thus giving vastly different resilience/distractibility profiles as a function of G. Given that, as it has been explained, the models are, anatomy apart, the same, this G profile difference is only due to the variations in anatomy across the species, giving us here an important network-distributed, complex system effect of structure on function, as no single change in the connectivity matrix can produce this behavioral difference on its own.

A second aspect of parametrization concerns the parameters J_s and J_{IE} which, albeit fixed for each area, will vary as a function of the available spine count gradient data. It is only fair to recognize that we have, at this date, less available data for the marmoset (**Table S2**. For non consensus data, see Theodoni et al. (2022), Supp. Table 4) regarding spine counts than we currently do for the macaque (**Table S1**). Therefore, if the models are indeed identical across our two species, the marmoset may be considered at this point less constrained than the macaque. New data, or data updates that would come in the future may very well change the present results, by making them more alike or more different, by reducing the window of distractibility of G or by expanding it. New macaque data could possibly create a band of distractibility on the G parameter line. This point, incidentally, is just as true for any change in the connectivity.

4.3. Scaling properties of the brain

The very low level of activity in macaque FEF and DP, compared to their marmoset counterparts, can be explained by the difference in connectivity for these areas across the two species. As we have argued elsewhere (Magrou et al., 2024), these anatomical differences can be thought in the framework

of the scaling properties of the brain. Indeed, due to physical constraints exerted onto the brain (Ringo, 1991), a bigger brain will get bigger only the cost of reducing its overall connectivity, which in turns leads to an increasing modularity of its network (Magrou et al., 2024; Changeux et al., 2021). This effect of scaling the brain up may well be at work here: the macaque and the marmoset 29×29 consensus connectivity matrices in **Figure 2** have a similar graph densities, although a 4% drop is already detectable from marmoset (0.72) to macaque (0.68). Additionally, **Figure 3A** clearly shows that the macaque's FLN range spans 6 orders of magnitude when the marmoset does only 5 (Theodoni et al., 2022; Markov et al., 2014a), meaning that the former possesses extra-weak connections compared to the latter. In short, the macaque brain is already about twice as big as the marmoset brain and, although it is still small enough to harbor a high graph density, it is already on its way to partial disconnection compared to its smaller cousin, as already shown elsewhere (Theodoni et al., 2022).

From a different perspective, Markov et al. (2014b) showed that FB connections decay with white matter distance more slowly than FF ones. This means that, on average, long-range, weak connections will tend to be FB. Extrapolating across species, we should expect the brain to — at least in primates — become increasingly FB-dominated as it grows larger. This aligns well with the data shown in **Figure 3B**, where the mean SLN value for the macaque is 0.47, which is non negligibly lower than the 0.59 of the marmoset, meaning that the macaque is on average more FB than the marmoset. Given the implementation of the CIB in the system, FB connections target the inhibitory population C, meaning that an on average more FB connectivity will lead to greater global inhibition. This is consistent with the macaque being resilient, as the random distractor will enter a system that is in effect less suited to its propagation. Conversely, the marmoset system is well suited to welcome the next distractor, its global feedforwardness effortlessly carrying its excitatory influence to all areas.

Circling back to macaque FEF and DP, these are arguably the deeper reasons why the macaque FEF and DP fail to display high levels of activity in our simulations. A bigger brain leads to some amount of disconnections — weaker connections or even missing ones — and greater feedbackness, which, in turn, leads to less input — although more selective — for these areas. From this, a conjecture could be that the same model grounded on a bigger brain's connectivity, such as that of a great ape or even a human primate, would see further disconnections and even greater feedbackness and

comparatively more areas behaving in that particular fashion. This, in turn, would be consistent with the increasing well segregated sub-network and functions that we see appear in bigger brains (Du et al., 2024; Magrou et al., 2024).

With respect the scaling up of the model to 29 areas (**Figure S7**), the enhanced stability given by the sheer number of areas forbids even the marmoset model to be sensitive to distraction. This points a limitation of this multiregional model which, due to its architecture, tends to be resilient to distraction already with two areas (Murray et al., 2017). The consequence of that is that the marmoset's 11 area model distractibility is very much non trivial. As scaling up the number of areas from 1 to 11 (or more) tends to lead to stability, it means that there is something very specific about the marmoset WM subnetwork's anatomy that manages to prevent said stability.

4.4. Distracted macaques and focused marmosets

As we saw with **Figure 5 and 6**, this system produces by default a macaque resilient to distraction and a marmoset sensitive to it, on par with the behavioral data available at this time (Joyce et al., 2024; Nakamura et al., 2018). The anatomical frontoparietal differences between macaque and marmoset, such as the missing connection between consensus marmoset areas A46D and LIP, known to be highly relevant for WM in the macaque ((Goldman-Rakic, 1992)), fail to explain the difference in behavior within the constraints of our model. Even the complete swapping of species specific connections from one to the other cannot achieve the intended behavioral reversal (**Figure S8**). This argues for the existence of an emergent stability produced by network-based complex system of non-linear interactions.

This stable default behavior can nonetheless be changed by regionally (*i.e.* DLPFC vs. PPC) altering the connectivity. The macaque becomes distractible by artificially scaling down the prefrontal self connectivity, coherently with previous work (Murray et al., 2017) and effectively making it less powerful at talking to itself and less prone to down-regulating parietal areas. This is consonant with experimental data, where PFC lesions increase distractibility in macaques (Suzuki and Gottlieb, 2013). On a more graph theoretical side, it can be thought of a way to reduce the prefrontal's modularity. Because this alone is enough to allow a distractor to win over the system and because the distractor signal comes from the parietal areas, this result can be interpreted as making the prefrontal more permeable to upward signal from the parietal.

In the marmoset's case, both intrafrontal and frontoparietal connections need to be tuned up to achieve resilience which, at a conceptual level, creates a nice and logical continuum between the two species. However, the opposition is imperfect. Were it to be perfect, an intrafrontal increase would have been enough to render the marmoset resilient. In practice, one needs to increase the frontoparietal connections (ρ_2) by a similar amount to complete the transition, as is shown in **Figure 7B**. Increasing the ρ_1 to 1.4 but keeping ρ_2 at 1 lead to a mixed regime where prefrontal areas are resilient but parietal areas remain sensitive to distractors**Figure S9C**. The likely interpretation is that, by increasing only intrafrontal connections, each prefrontal area now receives enough input from the other prefrontal areas that their collective activity is self-sustained and hard to break. We know from Murray et al. (2017) that resilience to distraction is given by the prefrontal module. For this new found capability to propagate to the rest of the system, one needs to increase the influence of prefrontal areas on the parietal, which is here modeled by increasing ρ_2.

This need of raising ρ_2 to complete the transition may come from the missing connections between marmoset area 46 (here A46D) and parietal areas LIP, OPt and PE_PEC (**Figure 4B**), given the importance of area 46 to WM (Goldman-Rakic, 1992). Although the marmoset possesses weak frontoparietal connections from A10 to the medial parietal cortex that the macaque does not (**Figure 4B**), these are unlikely to provide robust top-down control. Many substitutions of connections between the two species, analogous to grafting experiments, were tried in the course of this study, but no particular change in the matrix gave a clear cut answer. Incidentally, this is also true with respect to both SLNs and spine count interchanges. all theses are signatures of a complex system.

Now imagining the phase diagram shown in **Figure 8A** as a 3D energy landscape seen from above, becoming distractible here means that the wells that constitute population A and B stable points are getting shallower, with an increasingly reduced basin of attraction that can keep the system captive to that fixed point (*i.e.* the separatrix). As ρ_1 gradually decreases, so does the depth of the wells and the size of the separatrix. Thus, there is a point at which the distractor's energy is enough to escape ($\rho_1 \approx 0.64$), only to fall into the other fixed point's energy well.

The same is true for the marmoset, only reversed with respect to ρ_1. As the parameter increases (**Figure 8B**), the stable fixed points are gradually pulled deeper, increasing the basin of attraction in both size and gradient,

and making its separatrix gradually less escapable. starting at $\rho_1 \approx 1.065$, the energy wells are beginning to be too deep and/or too steep for any distractor to be able to push the system out of the well, and the system become resilient to distraction.

As can be seen in **Figure 7B** and further in **Figure 8**, the transition between distracted and resilient regimes is fairly sharp in both species, and leads to radically different qualitative results. In dynamical systems, this corresponds to the general definition of a bifurcation (Blanchard et al., 2012). As it does not appear to depend on local changes in the quality or quantity of stable or unstable fixed points, it should be better seen as a global bifurcation, although there are no limit cycle seemingly involved here. Nonetheless, the conceptual definition does seem to apply, as it appears obvious that some aspects of the high dimensional topology of the phase spaces in **Figure 8** are drastically changing over a very short span of ρ_1 values.

4.5. Working memory, ethology and evolution

From the bifurcation perspective hereabove, it appears that macaques and marmosets effectively sit on opposite sides of a common bifurcation. The particular side on which each species finds itself has been shaped by evolution and should relate to pertinent ecological and ethological aspects of their natural life. As further proof of this, the recent work of Joyce et al. (2024) have shown that marmoset DLPFC parvalbumin neurons have higher density of D1 (dopamine) receptors, which leads in their modeling to heightened susceptibility to distraction. Further, those levels are increasing from humans to marmosets, which in turn have similar levels to mice.

The first explanation that comes to mind is brain size, as we have made the case elsewhere that it is the prime factor that will allow for the sufficient segregation of functions, itself necessary for higher cognitive capabilities (Magrou et al., 2024). Further, and not unrelated, we explained earlier how weak, long range connections are tendentially more FB, leading to the expectation that larger brain should also be tendentially more FB, all things being otherwise equal. Another important ecological aspect to consider is their position in the trophic chain of their respective ecosystems. Indeed, by sheer size effect, the predatory difference may well select for heightened alertness in marmosets, which should in part rely on greater distractibility for either alarm calls from the group or direct sensory contact with a predator.

Finally, this distractibility difference aligns well with the differences at work in their social ethology. Where macaques heavily rely on aggression

and distrust (Balasubramaniam et al., 2012), marmosets are a highly collaborative species with respect to problem solving, a trait otherwise fairly restricted to apes (Sehner et al., 2022; Miller et al., 2016). In that particular context, distraction may be better seen as the local aspect of a larger, social information flow. Conversely, in a strict hierarchy of aggression, the necessity to efficiently navigate complex power dynamics, an individual macaque able to retain and manipulate information on their own, despite distractors coming from the group, would likely fare better than average.

An in depth research in social cognition, ethology and ecology would be necessary to untangle the complex web of selection pressures that may have shaped differentially our two species, and are far beyond the scope of this particular study. Additionally, Future modeling of the highly non-linear evolutionary dynamics at play here is necessary to deepen or knowledge of these interactions.

5. Conclusion

After producing a consensus mapping between macaque and marmoset's atlases, we reduced each to an homolog parcelation scheme, thus allowing direct, area-to-area comparison of their respective connectomes. We then used these consensus data to differentially constrain an otherwise identical large-scale model of WM. Selecting for the frontoparietal WM network of the same 11 common consensus areas in the two species, we first showed that these two systems produce sustainable activity throughout the network after a cue is sent in. We went on to test their resilience to distraction and discovered that, although the macaque-constrained model resists easily to distraction, the marmoset model readily switches and commits the newest cue to memory by propagating it to all areas, taking over as the new sustained activity. Moreover, the two species can be bridged by scaling up or down specific quadrants of their connectivity matrix, which effectively alters intrafrontal and frontoparietal influence over the system, allowing us to better understand the differences between those two primates. We argue that these behavioral differences between models align intriguingly well with real life behavioral difference that could well be adaptative traits in response to specific aspects of their respective social ethology and ecology. Future modeling of evolutionary dynamics could prove useful in disentangling the links between structure, function, and ecologically relevant behaviors.

eTOC blurb/in brief

After making macaque and marmoset inter-areal connectome directly comparable through consensus mapping, the authors modeled both species by a large-scale model of working memory, which differed only by the two species' anatomy. The models sensibility to distraction captures real-life ethological differences between the two species of primates.

Acknowledgements

The Authors would like to thank Jorge Mejias for providing the base code and helpful advices along the way, the Wang lab for the constant challenges and discussions that helped build this paper, in particular Aldo Battista and Wayne Soo for so gracefully teaching their impressive mathematical knowledge. We would also like to thank Seán Froudist-Walsh and Mary Kate P. Joyce for the helpful discussions on the marmoset neurophysiology and behavior. This work was made possible thanks to the NSF NeuroNex grant 2015276 to A.F.T.A. and X-J.W.; the NIH grant R01MH062349 to X-J.W.; the Simons Foundation grant 543057SPI to X-J.W.; the National Health and Medical Research Council grant APP1194206 to M.G.P.R; the Australian Research Council grant DP210101042 to M.G.P.R; and the Australian Research Council Grant DP210103865 to M.G.P.R.

Author contribution

Conceptualization, L.M., P.T., M.G.P.R, X-J.W. ; methodology, L.M., P.T., M.G.P.R, X-J.W.; software, L.M.; validation, L.M., P.T., M.G.P.R, X-J.W.; formal analysis, L.M.; investigation, L.M., P.T., A.F.T.A., X-J.W.; resources, L.M., M.G.P.R., X-J.W.; writing – original draft, L.M.; writing – review & editing, all authors; visualization, L.M., P.T.; supervision, X-J.W; funding acquisition, A.F.T.A., M.G.P.R., X-J.W.

Main figures

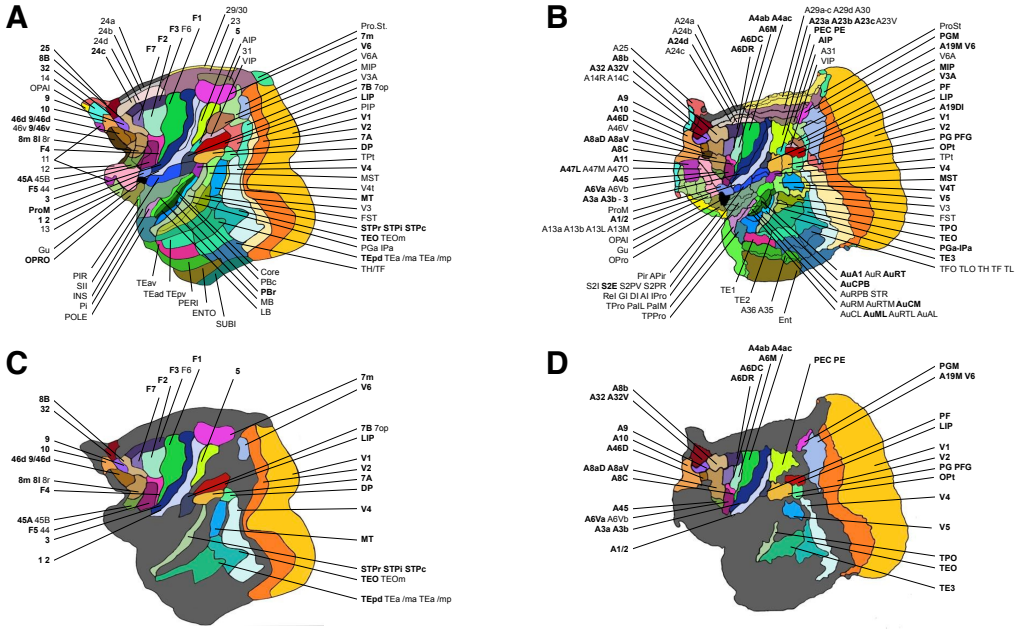

Figure 1: Flattened illustrations of the consensus mapping. **(A)** Macaque original 91 area atlas from Markov et al. (2014a). **(B)** Marmoset original 116 area atlas from Theodoni et al. (2022). **(C)** Macaque 29 consensus areas commonly injected with the marmoset. **(D)** Marmoset 29 homolog consensus areas from (C), commonly injected with the macaque. Area names placed on the same line represent areas that will be aggregated as one area by the consensus mapping, and are shown as separate areas of identical color in (A) and (B), and then fused in (C) and (D). Names in bold are those for which there at least one injection the the original connectivity dataset. For easiness of read, area labels are identically ordered between macaque (A and C) and marmoset (B and D). The full table of consensus equivalence across the two species is available in **Table S3**.

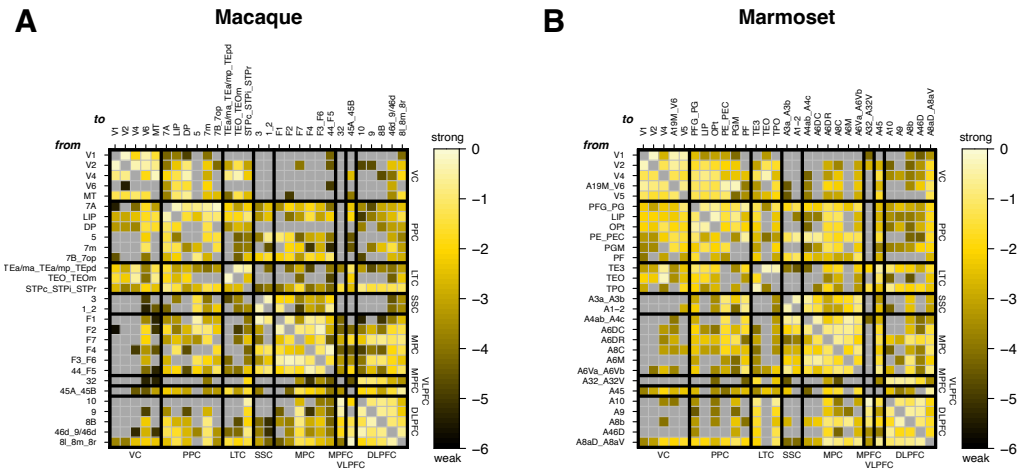

Figure 2: 29×29 common consensus log_{10} FLN matrices for both species. (A) Macaque **(B)** Marmoset. In these, each square of color represents a connection from source areas as rows to target areas as columns. Colors vary according to log_{10} FLN values, from very weak (black) to very strong (whitish yellow). Grey is the background color of the matrices and a grey square therefore identifies an absent connection. Black thicker lines separate brain regions, see **Table S3** for a key to regional acronyms. Areas merged by consensus are labeled by concatenating together the names of the original parcelation areas, separated by an underscore. Thanks to consensus, each connection are here one-to-one comparable across species. The corresponding SLN matrices are available in **Figure S4**, and a comprehensive connectivity table with both FLN and SLN values can be found in **Table S3**.

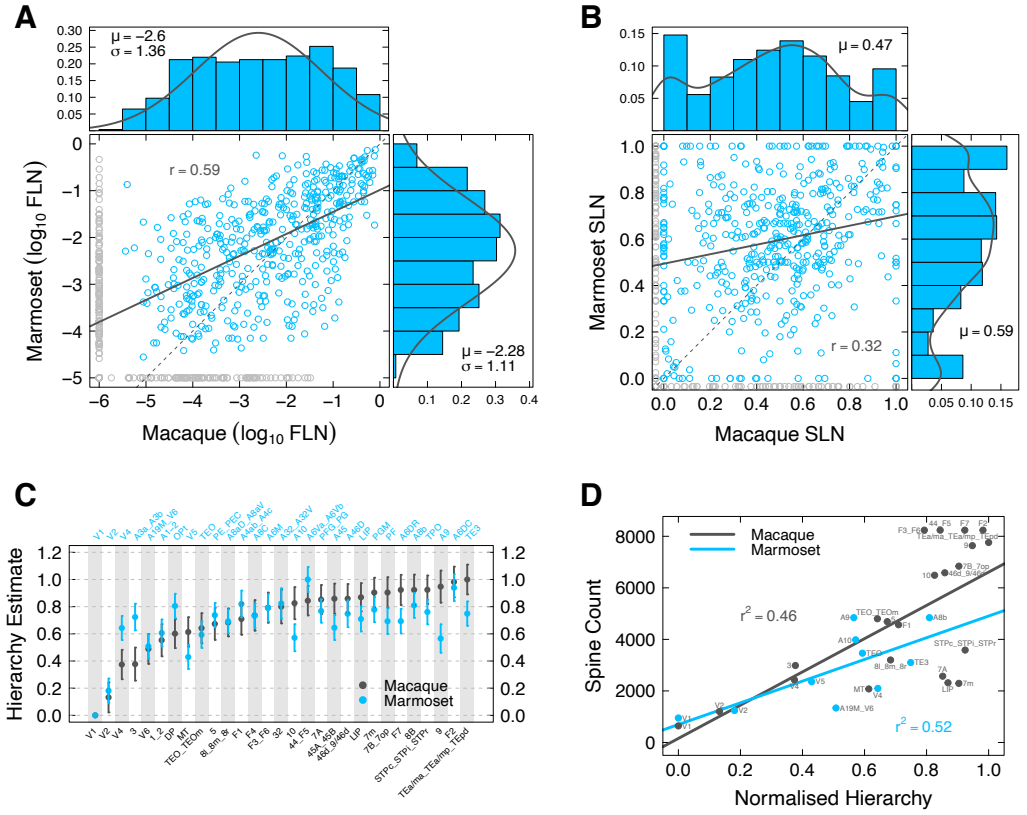

Figure 3: 29×29 Connectome statistics, SLN-based hierarchy estimates and spine counts. (A) Macaque (horizontal axis) vs marmoset (vertical axis) consensus log_{10} FLN correlation and distribution. In the main plot, each circle represent a connection. Blue, the connection exists in both species; grey, the connection exists in only one species. Solid black line, linear regression line between macaque and marmoset log_{10} FLNs, excluding grey datapoints; correlation coefficient of the regression line $r = 0.59$; thin broken line, line of unit slope for visual reference. In the top plot is the log_{10} FLN distribution for the macaque, including connections unique to the macaque; mean $\mu = -2.6$ and standard deviation $\sigma = 1.36$, used as parameters for the superimposed black normal curve. The same statistics are shown in the left plot for the marmoset, the same conventions apply. **(B)** Macaque (horizontal axis) vs marmoset (vertical axis) consensus SLN correlation and distribution. Same reading conventions as in (A). **(C)** SLN-based hierarchical estimates for macaque (black dots) and marmoset (blue dots), computed by a GLM of the beta-binomial family, using a logit link function. Values are ordered by macaque increasing estimates. Bottom axis, macaque consensus areas; top axis, marmoset homolog consensus areas. **(D)** Spine count as a function of normalized SLN-based hierarchy. Black dots and regression line, macaque; blue dots and regression line, marmoset. Proportion of variance explained r^2 is 0.46 for the macaque and 0.52 for the marmoset.

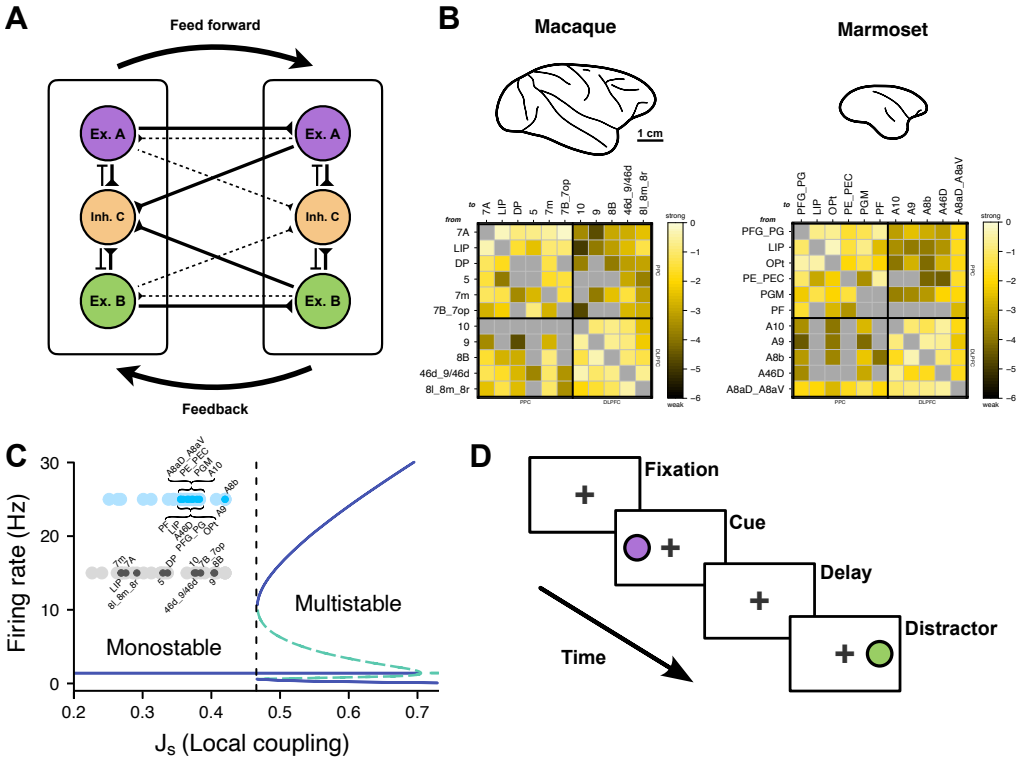

Figure 4: Large Scale model of distributed working memory. **(A)** schematic of the local circuit and inter-areal interactions. The local circuitry follows a standard 3-population Wong-&-Wang model (Wong and Wang, 2006), with 2 excitatory populations (ex. A and ex. B, purple and green) and 1 inhibitory population (inh. C, orange). Locally, populations A and B excites C which inhibits them in return; globally, inter-areal interactions are based on FLN and SLN anatomical data. **(B)** Comparative visual showing the macaque and marmoset brains at the same scale; scale bar, 1 cm. Under, the 11×11 submatrices that will be used the WM modeling. PPC, Posterior Parietal Cortex; DLPFC, Dorsal Lateral PreFrontal Cortex. Reading conventions identical to figure 2. **(C)** bifurcation diagram for an isolated area, with firing rates (Hz) as a function of parameter J_s. Below a certain threshold value of J_s, a single area cannot sustain long term activity and are monostable. Areas are all parametrized to fall below that threshold. Small dark grey dots corresponds to each of the 11 macaque areas from (B) and indicate their particular J_s values, larger pale grey dots represent the distribution of the rest of the 29 common consensus areas. Regular and pal blue dots assume the same function with respect to the marmoset. **(D)** Schematic representation of the WM task time course. After a 1 second fixation period, the cue is presented for 0.5 s (purple disk), in the form of a pulse of 0.3 nA sent to population A. After a delay period of 3 s, the distractor is presented (green disk) as a pulse to population B identical in time and intensity to the cue.

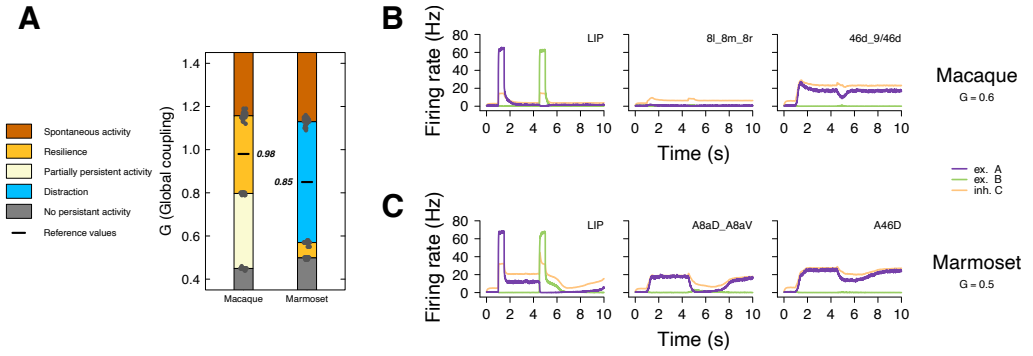

Figure 5: Parametrization of global coupling parameter G. **(A)** Stacked histogram showing different regimes of activity as a function of G, for both species. Dark orange, spontaneous activity; yellow, resilience to distraction; pale yellow, partially persistent activity; blue, distraction; dark grey, no persistent activity, black little, reference (chosen) value. Simulations were run with incremental G steps 0.01, with 20 different random seeds (black dots). Boundaries between regimes are computed as averages over all seeds at each qualitative change of regime. Reference value for each species is defined as the half point in the resilience regime for the macaque and the distracted regime for the marmoset. **(B)** Firing rate as a function of time for the macaque's partially persistent regime at $G = 0.6$. Purple trace, excitatory population A; green trace, excitatory population B; orange trace, inhibitory population C. Areas have been selectively chosen to showcase the partialness of this regime, with parietal areas not sustaining activity (LIP) whilst prefrontal areas do (46d_9/46d). Consensus area 8l_8m_8r (FEF) is shown as the one prefrontal area not following this logic. **(C)** Example behavior for the marmoset's small window of resilient regime at $G = 0.5$, where population A re-establishes itself after the distractor pulse. Homolog consensus areas and reading conventions as in (B). Complete set for (B) and (C) available in **Figure S6A and B**.

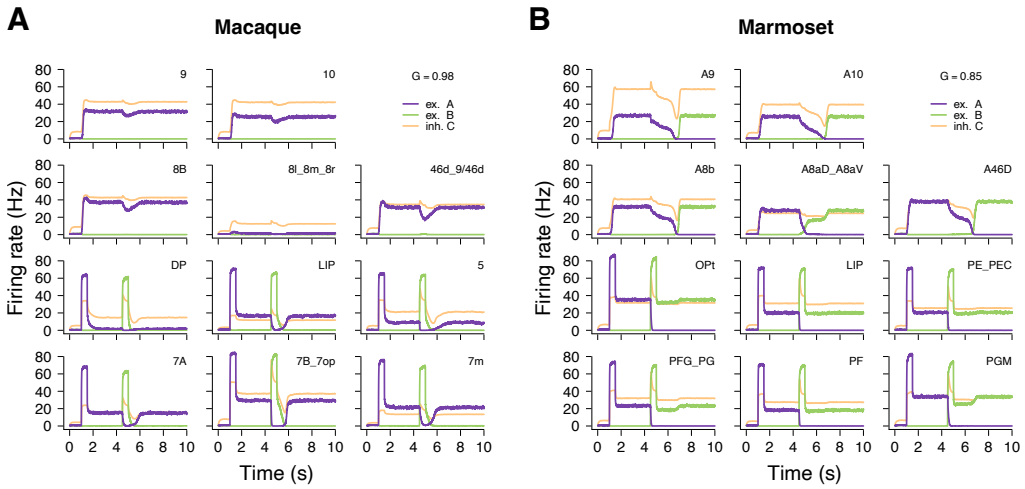

Figure 6: Standard behavior of the distributed frontoparietal working memory model. Each subplot shows the activity traces of the firing rates as a function of time for each of the 11 consensus areas of the selected frontoparietal network. Areas are directly comparable with their homolog and are placed accordingly. Cues ($t = 1$ s to population A, purple trace) and distractors ($t = 4.5$ s to population B, green trace) are sent to all parietal areas. Orange trace is inhibitory population C. **(A)** Macaque; global coupling parameter $G = 0.98$, resilient regime. **(B)** Marmoset; $G = 0.85$, distractible regime.

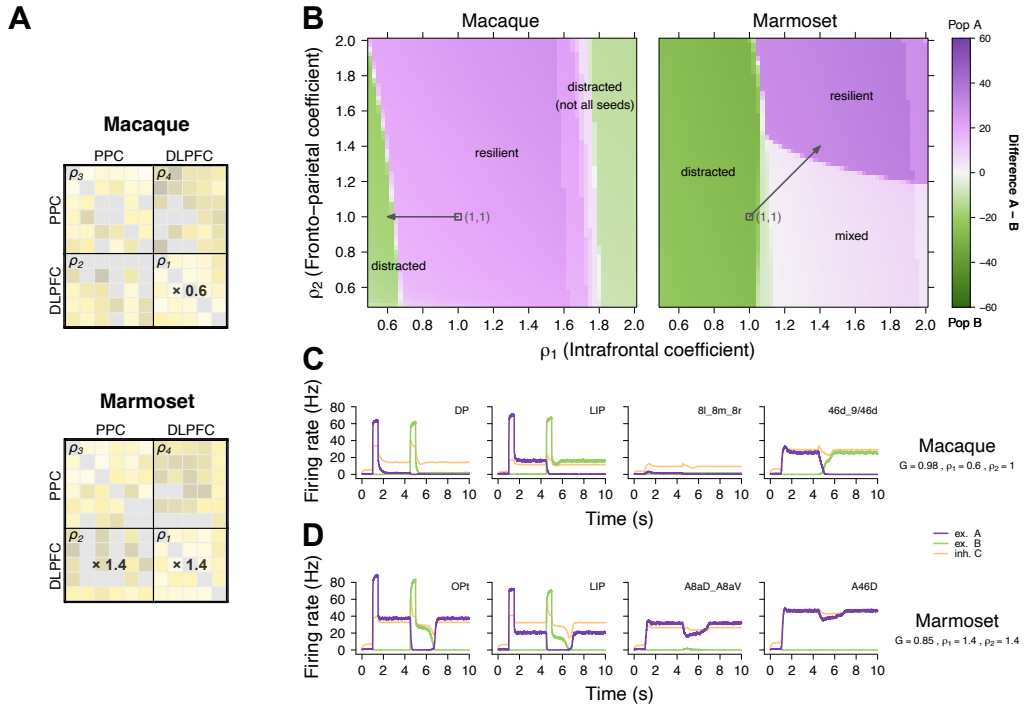

Figure 7: Parameter space analysis of resilience and distractibility. **(A)** 11×11 matrices from **Figure 3B** divided in four quadrants: ρ_1, DLPFC to DLPFC or intrafrontal; ρ_2, DLPFC to PPC or frontoparietal; ρ_3, PPC to PPC or intraparietal; ρ_4, PPC to DLPFC or parietofrontal. Setting ρ_1 to 0.6 in the macaque makes it sensitive to distraction. Setting ρ_1 and ρ_2 to 1.4 in the marmoset makes the system resilient. **(B)** ρ_1-ρ_2 parameter plane for both macaque (left panel) and marmoset (right panel). Green hues indicate resilient territories in the plane, purple hues indicate distracted, and white indicates mixed behavior (see **Figure S6C**). Each square is the average of simulations performed over 10 different random seeds, by incremental steps of 0.025 in both directions. Black open squares indicate (1,1) coordinates in the plane, black arrows indicate the displacements generated by values in (A). **(C)** Example behavior for the macaque's distractible regime at $G = 0.98,\ \rho_1 = 0.6,\ \rho_2 = 1$. **(D)** Example behavior for the marmoset's resilient regime at $G = 0.85,\ \rho_1 = 1.4,\ \rho_2 = 1.4$. Reading conventions as in **Figure 5B and C**. Complete set for (C) and (D) available in **Figure S9A and B**.

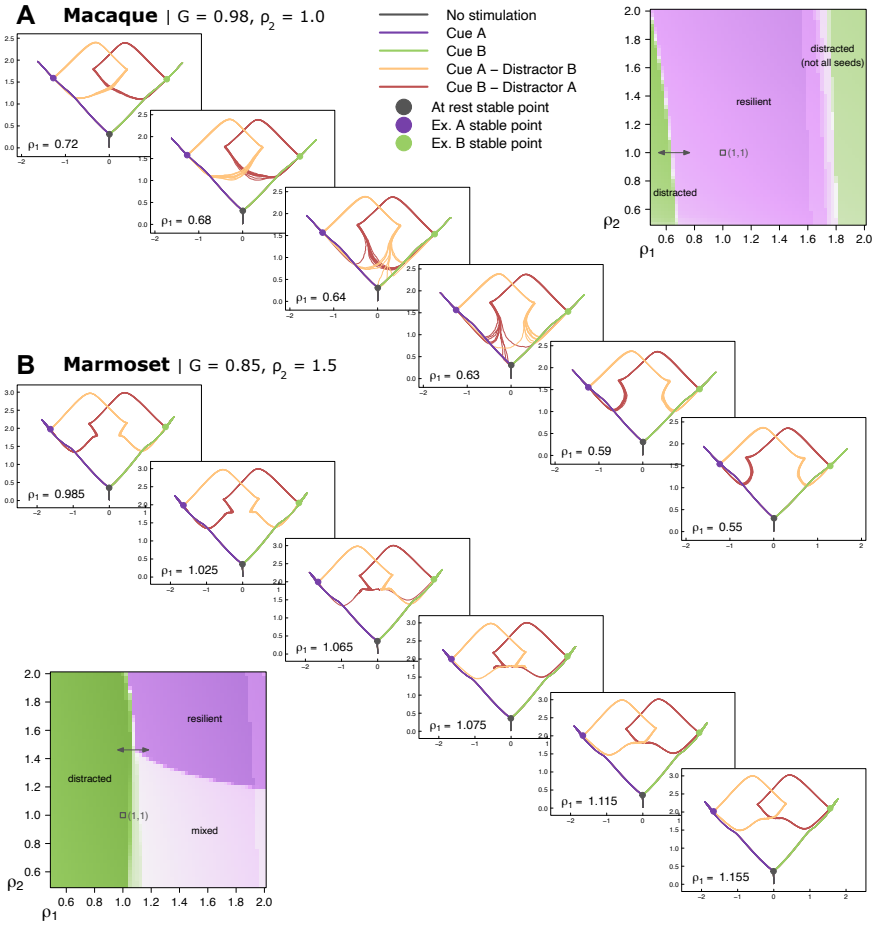

Figure 8: S_A-S_B conductance phase space gradual change across regime boundaries. The plane is chosen as the unique plane defined by the 3 stable fixed points of the system, then rotated by $\pi/4$ for visual clarity. Colored dots indicate said fixed points: black, at rest (no input current); purple, population A; green, population B. Colored lines follow the same convention for trajectories: black, at rest (no input current); purple, cue input current in population A; green, cue input current in population B; yellow, distractor input current in population B when at stable fixed point A; dark red, distractor input current in population A when at stable fixed point B. Trajectories computed for 10 different random seeds for all conditions. **(A)** Macaque. Each plot corresponds to an incremental step in ρ_1, starting from a resilient macaque. Parameters G and ρ_2 are fixed at 0.98 and 1 respectively. Full investigated range from $\rho_1 = 0.75$ to $\rho_1 = 0.55$ with 0.01 step size, available in **Video S1A**. **(B)** Marmoset. Each plot corresponds to an incremental step in ρ_1, starting from a distractible marmoset. Parameters G and ρ_2 are fixed at 0.85 and 1.5 respectively. Full investigated range from $\rho_1 = 0.975$ to $\rho_1 = 1.175$ with 0.01 step size, available in **Video S1B**. For each species, inset plots help visualize the covered range of values in ρ_1-ρ_2 parameter space.

References

Abbott, L.F., Chance, F.S., 2005. Drivers and modulators from push-pull and balanced synaptic input. Progress in brain research 149, 147–155.

Bakola, S., Burman, K.J., Rosa, M.G., 2015. The cortical motor system of the marmoset monkey (callithrix jacchus). Neuroscience research 93, 72–81.

Balasubramaniam, K.N., Dittmar, K., Berman, C.M., Butovskaya, M., Cooper, M.A., Majolo, B., Ogawa, H., Schino, G., Thierry, B., De Waal, F.B., 2012. Hierarchical steepness, counter-aggression, and macaque social style scale. American journal of primatology 74, 915–925.

Barone, P., Batardiere, A., Knoblauch, K., Kennedy, H., 2000. Laminar distribution of neurons in extrastriate areas projecting to visual areas v1 and v4 correlates with the hierarchical rank and indicates the operation of a distance rule. Journal of Neuroscience 20, 3263–3281.

Binzegger, T., Douglas, R.J., Martin, K.A., 2004. A quantitative map of the circuit of cat primary visual cortex. Journal of Neuroscience 24, 8441–8453.

Binzegger, T., Douglas, R.J., Martin, K.A., 2009. Topology and dynamics of the canonical circuit of cat v1. Neural Networks 22, 1071–1078.

Blanchard, P., Devaney, R., Hall, G., 2012. Differential Equations. Cengage Learning.

Chafee, M.V., Goldman-Rakic, P.S., 1998. Matching patterns of activity in primate prefrontal area 8a and parietal area 7ip neurons during a spatial working memorytask. Journal of neurophysiology 79, 2919–2940.

Changeux, J.P., Goulas, A., Hilgetag, C.C., 2021. A connectomic hypothesis for the hominization of the brain. Cerebral cortex 31, 2425–2449.

Chaudhuri, R., Knoblauch, K., Gariel, M.A., Kennedy, H., Wang, X.J., 2015. A large-scale circuit mechanism for hierarchical dynamical processing in the primate cortex. Neuron 88, 419–431.

Christophel, T.B., Klink, P.C., Spitzer, B., Roelfsema, P.R., Haynes, J.D., 2017. The distributed nature of working memory. Trends in cognitive sciences 21, 111–124.

Consagra, W., Venkataraman, A., Zhang, Z., 2022. Optimized diffusion imaging for brain structural connectome analysis. IEEE transactions on medical imaging 41, 2118–2129.

Delhaye, B.P., Long, K.H., Bensmaia, S.J., 2018. Neural basis of touch and proprioception in primate cortex. Comprehensive Physiology 8, 1575.

Donahue, C.J., Sotiropoulos, S.N., Jbabdi, S., Hernandez-Fernandez, M., Behrens, T.E., Dyrby, T.B., Coalson, T., Kennedy, H., Knoblauch, K., Van Essen, D.C., et al., 2016. Using diffusion tractography to predict cortical connection strength and distance: a quantitative comparison with tracers in the monkey. Journal of Neuroscience 36, 6758–6770.

Dorkenwald, S., McKellar, C.E., Macrina, T., Kemnitz, N., Lee, K., Lu, R., Wu, J., Popovych, S., Mitchell, E., Nehoran, B., et al., 2022. Flywire: online community for whole-brain connectomics. Nature methods 19, 119–128.

Douglas, R.J., Martin, K.A., Whitteridge, D., 1989. A canonical microcircuit for neocortex. Neural computation 1, 480–488.

Du, J., DiNicola, L.M., Angeli, P.A., Saadon-Grosman, N., Sun, W., Kaiser, S., Ladopoulou, J., Xue, A., Yeo, B.T., Eldaief, M.C., et al., 2024. Organization of the human cerebral cortex estimated within individuals: networks, global topography, and function. Journal of Neurophysiology 131, 1014–1082.

Elston, G., 2001. Interlaminar differences in the pyramidal cell phenotype in cortical areas 7m and stp (the superior temporal polysensory area) of the macaque monkey. Experimental brain research 138, 141–152.

Elston, G.N., 2007. Specialization of the neocortical pyramidal cell during primate evolution. Evolution of nervous systems , 191–242.

Elston, G.N., Benavides-Piccione, R., DeFelipe, J., 2001. The pyramidal cell in cognition: a comparative study in human and monkey. The Journal of Neuroscience 21, RC163.

Elston, G.N., Benavides-Piccione, R., Elston, A., Manger, P.R., DeFelipe, J., 2011. Pyramidal cells in prefrontal cortex of primates: marked differences in neuronal structure among species. Front. Neuroanat. 5, 2.

Elston, G.N., Oga, T., Fujita, I., 2009. Spinogenesis and pruning scales across functional hierarchies. Journal of Neuroscience 29, 3271–3275.

Elston, G.N., Oga, T., Okamoto, T., Fujita, I., 2010. Spinogenesis and pruning from early visual onset to adulthood: an intracellular injection study of layer iii pyramidal cells in the ventral visual cortical pathway of the macaque monkey. Cerebral Cortex 20, 1398–1408.

Elston, G.N., Rockland, K.S., 2002. The pyramidal cell of the sensorimotor cortex of the macaque monkey: phenotypic variation. Cerebral Cortex 12, 1071–1078.

Elston, G.N., Rosa, M., 1997. The occipitoparietal pathway of the macaque monkey: comparison of pyramidal cell morphology in layer iii of functionally related cortical visual areas. Cerebral cortex (New York, NY: 1991) 7, 432–452.

Elston, G.N., Rosa, M., 1998a. Morphological variation of layer iii pyramidal neurones in the occipitotemporal pathway of the macaque monkey visual cortex. Cerebral cortex (New York, NY: 1991) 8, 278–294.

Elston, G.N., Rosa, M.G., 1998b. Complex dendritic fields of pyramidal cells in the frontal eye field of the macaque monkey: comparison with parietal areas 7a and lip. Neuroreport 9, 127–131.

Elston, G.N., Tweedale, R., Rosa, M.G., 1999a. Cellular heterogeneity in cerebral cortex: a study of the morphology of pyramidal neurones in visual areas of the marmoset monkey. Journal of Comparative Neurology 415, 33–51.

Elston, G.N., Tweedale, R., Rosa, M.G.P., 1999b. Cortical integration in the visual system of the macaque monkey: large-scale morphological differences in the pyramidal neurons in the occipital, parietal and temporal lobes. Proceedings of the Royal Society of London. Series B: Biological Sciences 266, 1367–1374.

Ercsey-Ravasz, M., Markov, N.T., Lamy, C., Van Essen, D.C., Knoblauch, K., Toroczkai, Z., Kennedy, H., 2013. A predictive network model of cerebral cortical connectivity based on a distance rule. Neuron 80, 184–197.

Falchier, A., Clavagnier, S., Barone, P., Kennedy, H., 2002. Anatomical evidence of multimodal integration in primate striate cortex. Journal of Neuroscience 22, 5749–5759.

Felleman, D.J., Van Essen, D.C., 1991. Distributed hierarchical processing in the primate cerebral cortex. Cerebral cortex (New York, NY: 1991) 1, 1–47.

Froudist-Walsh, S., Bliss, D.P., Ding, X., Rapan, L., Niu, M., Knoblauch, K., Zilles, K., Kennedy, H., Palomero-Gallagher, N., Wang, X.J., 2021. A dopamine gradient controls access to distributed working memory in the large-scale monkey cortex. Neuron 109, 3500–3520.

Froudist-Walsh, S., Xu, T., Niu, M., Rapan, L., Zhao, L., Margulies, D.S., Zilles, K., Wang, X.J., Palomero-Gallagher, N., 2023. Gradients of neurotransmitter receptor expression in the macaque cortex. Nature neuroscience 26, 1281–1294.

Fuster, J.M., Alexander, G.E., 1971. Neuron activity related to short-term memory. Science 173, 652–654.

Gajwani, M., Oldham, S., Pang, J.C., Arnatkevičiūtė, A., Tiego, J., Bellgrove, M.A., Fornito, A., 2023. Can hubs of the human connectome be identified consistently with diffusion mri? Network Neuroscience 7, 1326–1350.

Gămănuţ, R., Kennedy, H., Toroczkai, Z., Ercsey-Ravasz, M., Van Essen, D.C., Knoblauch, K., Burkhalter, A., 2018. The mouse cortical connectome, characterized by an ultra-dense cortical graph, maintains specificity by distinct connectivity profiles. Neuron 97, 698–715.

Girard, P., Bullier, J., 1989. Visual activity in area v2 during reversible inactivation of area 17 in the macaque monkey. Journal of neurophysiology 62, 1287–1302.

Goldman-Rakic, P.S., 1992. Working memory and the mind. Scientific American 267, 110–117.

Hagmann, P., 2005. From diffusion MRI to brain connectomics. Ph.D. thesis. École Polytechnique Fédérale de Lausanne (EPFL).

Harris, J.A., Mihalas, S., Hirokawa, K.E., Whitesell, J.D., Choi, H., Bernard, A., Bohn, P., Caldejon, S., Casal, L., Cho, A., et al., 2019. Hierarchical organization of cortical and thalamic connectivity. Nature 575, 195–202.

Harris, K.D., Mrsic-Flogel, T.D., 2013. Cortical connectivity and sensory coding. Nature 503, 51–58.

Horvát, S., Gămănuț, R., Ercsey-Ravasz, M., Magrou, L., Gămănuț, B., Van Essen, D.C., Burkhalter, A., Knoblauch, K., Toroczkai, Z., Kennedy, H., 2016. Spatial embedding and wiring cost constrain the functional layout of the cortical network of rodents and primates. PLoS biology 14, e1002512.

Hupé, J., James, A., Payne, B., Lomber, S., Girard, P., Bullier, J., 1998. Cortical feedback improves discrimination between figure and background by v1, v2 and v3 neurons. Nature 394, 784–787.

Joyce, M.K.P., Ivanov, T.G., Krienen, F., Mitchell, J., Ma, S., Inoue, W., Nandy, A.P., Datta, D., Duque, A., Arellano, J.I., et al., 2024. Dopamine d1 receptor expression in dlpfc inhibitory parvalbumin neurons may contribute to higher visuospatial distractibility in marmosets versus macaques. bioRxiv , 2024–06.

Leavitt, M.L., Mendoza-Halliday, D., Martinez-Trujillo, J.C., 2017. Sustained activity encoding working memories: not fully distributed. Trends in Neurosciences 40, 328–346.

Lorenc, E.S., Mallett, R., Lewis-Peacock, J.A., 2021. Distraction in visual working memory: Resistance is not futile. Trends in cognitive sciences 25, 228–239.

Magrou, L., Joyce, M.K.P., Froudist-Walsh, S., Datta, D., Wang, X.J., Martinez-Trujillo, J., Arnsten, A.F., 2024. The meso-connectomes of mouse, marmoset, and macaque: network organization and the emergence of higher cognition. Cerebral Cortex 34, bhae174.

Majka, P., Bai, S., Bakola, S., Bednarek, S., Chan, J.M., Jermakow, N., Passarelli, L., Reser, D.H., Theodoni, P., Worthy, K.H., et al., 2020. Open access resource for cellular-resolution analyses of corticocortical connectivity in the marmoset monkey. Nature communications 11, 1133.

Markov, N.T., Ercsey-Ravasz, M., Van Essen, D.C., Knoblauch, K., Toroczkai, Z., Kennedy, H., 2013. Cortical high-density counterstream architectures. Science 342, 1238406.

Markov, N.T., Ercsey-Ravasz, M.M., Ribeiro Gomes, A., Lamy, C., Magrou, L., Vezoli, J., Misery, P., Falchier, A., Quilodran, R., Gariel, M.A., et al., 2014a. A weighted and directed interareal connectivity matrix for macaque cerebral cortex. Cerebral cortex 24, 17–36.

Markov, N.T., Misery, P., Falchier, A., Lamy, C., Vezoli, J., Quilodran, R., Gariel, M., Giroud, P., Ercsey-Ravasz, M., Pilaz, L., et al., 2011. Weight consistency specifies regularities of macaque cortical networks. Cerebral cortex 21, 1254–1272.

Markov, N.T., Vezoli, J., Chameau, P., Falchier, A., Quilodran, R., Huissoud, C., Lamy, C., Misery, P., Giroud, P., Ullman, S., et al., 2014b. Anatomy of hierarchy: feedforward and feedback pathways in macaque visual cortex. Journal of comparative neurology 522, 225–259.

Mayr, E., 1982. The Growth of Biological Thought: Diversity, Evolution, and Inheritance. Belknap Press.

Mejias, J.F., Wang, X.J., 2022. Mechanisms of distributed working memory in a large-scale network of macaque neocortex. Elife 11, e72136.

Miller, C.T., Freiwald, W.A., Leopold, D.A., Mitchell, J.F., Silva, A.C., Wang, X., 2016. Marmosets: a neuroscientific model of human social behavior. Neuron 90, 219–233.

Mitchell, J.F., Leopold, D.A., 2015. The marmoset monkey as a model for visual neuroscience. Neuroscience research 93, 20–46.

Murray, J.D., Jaramillo, J., Wang, X.J., 2017. Working memory and decision-making in a frontoparietal circuit model. Journal of Neuroscience 37, 12167–12186.

Murre, J.M., Sturdy, D.P., 1995. The connectivity of the brain: multi-level quantitative analysis. Biological cybernetics 73, 529–545.

Nakamura, K., Koba, R., Miwa, M., Yamaguchi, C., Suzuki, H., Takemoto, A., 2018. A method to train marmosets in visual working memory task and their performance. Frontiers in behavioral neuroscience 12, 46.

Nimchinsky, E.A., Sabatini, B.L., Svoboda, K., 2002. Structure and function of dendritic spines. Annual review of physiology 64, 313–353.

Oga, T., Aoi, H., Sasaki, T., Fujita, I., Ichinohe, N., 2013. Postnatal development of layer iii pyramidal cells in the primary visual, inferior temporal, and prefrontal cortices of the marmoset. Frontiers in neural circuits 7, 31.

Okano, H., Hikishima, K., Iriki, A., Sasaki, E., 2012. The common marmoset as a novel animal model system for biomedical and neuroscience research applications, in: Seminars in fetal and neonatal medicine, Elsevier. pp. 336–340.

Olesen, P.J., Macoveanu, J., Tegnér, J., Klingberg, T., 2007. Brain activity related to working memory and distraction in children and adults. Cerebral cortex 17, 1047–1054.

Paxinos, G., Watson, C., Petrides, M., Rosa, M., Tokuno, H., 2012. The marmoset brain in stereotaxic coordinates. Elsevier Academic Press.

Prins, N.W., Pohlmeyer, E.A., Debnath, S., Mylavarapu, R., Geng, S., Sanchez, J.C., Rothen, D., Prasad, A., 2017. Common marmoset (callithrix jacchus) as a primate model for behavioral neuroscience studies. Journal of neuroscience methods 284, 35–46.

Reser, D.H., Burman, K.J., Yu, H.H., Chaplin, T.A., Richardson, K.E., Worthy, K.H., Rosa, M.G., 2013. Contrasting patterns of cortical input to architectural subdivisions of the area 8 complex: a retrograde tracing study in marmoset monkeys. Cerebral Cortex 23, 1901–1922.

Ringo, J.L., 1991. Neuronal interconnection as a function of brain size. Brain, behavior and evolution 38, 1–6.

Rockland, K.S., Pandya, D.N., 1979. Laminar origins and terminations of cortical connections of the occipital lobe in the rhesus monkey. Brain research 179, 3–20.

Sasaki, T., Aoi, H., Oga, T., Fujita, I., Ichinohe, N., 2015. Postnatal development of dendritic structure of layer iii pyramidal neurons in the medial prefrontal cortex of marmoset. Brain Structure and Function 220, 3245–3258.

Scheffer, L.K., Xu, C.S., Januszewski, M., Lu, Z., Takemura, S.y., Hayworth, K.J., Huang, G.B., Shinomiya, K., Maitlin-Shepard, J., Berg, S., et al., 2020. A connectome and analysis of the adult drosophila central brain. elife 9, e57443.

Sehner, S., Willems, E.P., Vinicus, L., Migliano, A.B., van Schaik, C.P., Burkart, J.M., 2022. Problem-solving in groups of common marmosets (callithrix jacchus): more than the sum of its parts. PNAS nexus 1, pgac168.

Solomon, S.G., Rosa, M.G., 2014. A simpler primate brain: the visual system of the marmoset monkey. Frontiers in neural circuits 8, 96.

Sporns, O., Tononi, G., Kötter, R., 2005. The human connectome: a structural description of the human brain. PLoS computational biology 1, e42.

Sreenivasan, K.K., D'Esposito, M., 2019. The what, where and how of delay activity. Nature reviews neuroscience 20, 466–481.

Suzuki, M., Gottlieb, J., 2013. Distinct neural mechanisms of distractor suppression in the frontal and parietal lobe. Nature neuroscience 16, 98–104.

Theodoni, P., Majka, P., Reser, D.H., Wójcik, D.K., Rosa, M.G., Wang, X.J., 2022. Structural attributes and principles of the neocortical connectome in the marmoset monkey. Cerebral Cortex 32, 15–28.

Tsushima, Y., Sasaki, Y., Watanabe, T., 2006. Greater disruption due to failure of inhibitory control on an ambiguous distractor. Science 314, 1786–1788.

Van Essen, D.C., Maunsell, J.H., 1983. Hierarchical organization and functional streams in the visual cortex. Trends in neurosciences 6, 370–375.

Vezoli, J., Magrou, L., Goebel, R., Wang, X.J., Knoblauch, K., Vinck, M., Kennedy, H., 2021. Cortical hierarchy, dual counterstream architecture and the importance of top-down generative networks. Neuroimage 225, 117479.

Wang, X.J., 2001. Synaptic reverberation underlying mnemonic persistent activity. Trends in neurosciences 24, 455–463.

Wang, X.J., 2021. 50 years of mnemonic persistent activity: quo vadis? Trends in Neurosciences 44, 888–902.

Wang, X.J., 2022. Theory of the multiregional neocortex: large-scale neural dynamics and distributed cognition. Annual review of neuroscience 45, 533–560.

Wang, X.J., Kennedy, H., 2016. Brain structure and dynamics across scales: in search of rules. Current opinion in neurobiology 37, 92–98.

Wong, K.F., Wang, X.J., 2006. A recurrent network mechanism of time integration in perceptual decisions. Journal of Neuroscience 26, 1314–1328.

Wong, R.K., Selvanayagam, J., Johnston, K.D., Everling, S., 2023. Delay-related activity in marmoset prefrontal cortex. Cerebral Cortex 33, 3523–3537.

Supplementary information

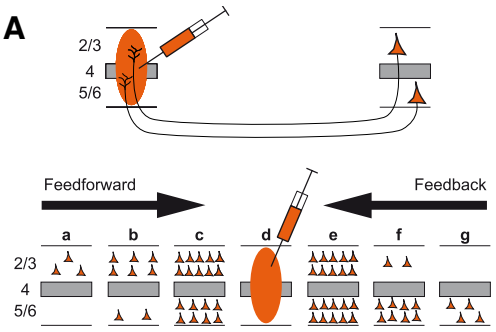

B

$$FLN_{b \to d} = \frac{N \text{ neurones in } b}{\sum \text{ neurones in all areas}}$$

$$SLN_{b \to d} = \frac{N \text{ supragranular neurones in } b}{N \text{ neurones in } b}$$

Figure S1: Retrograde tract tracing and connectivity computations. **(A)** In retrograde tract tracing, the tracer is captured by axon terminals present in the uptake zone (orange oval) and actively transported back to the soma of the cells. FF connections (*i.e.* from lower hierarchical levels) originates predominantly in the supragranular layers, a dominance that becomes gradually more apparent as hierarchical distance increases. The converse is symmetrically true for FBs and infragranular layers. **(B)** FLN and SLN equations to compute both metrics for each existing connection.

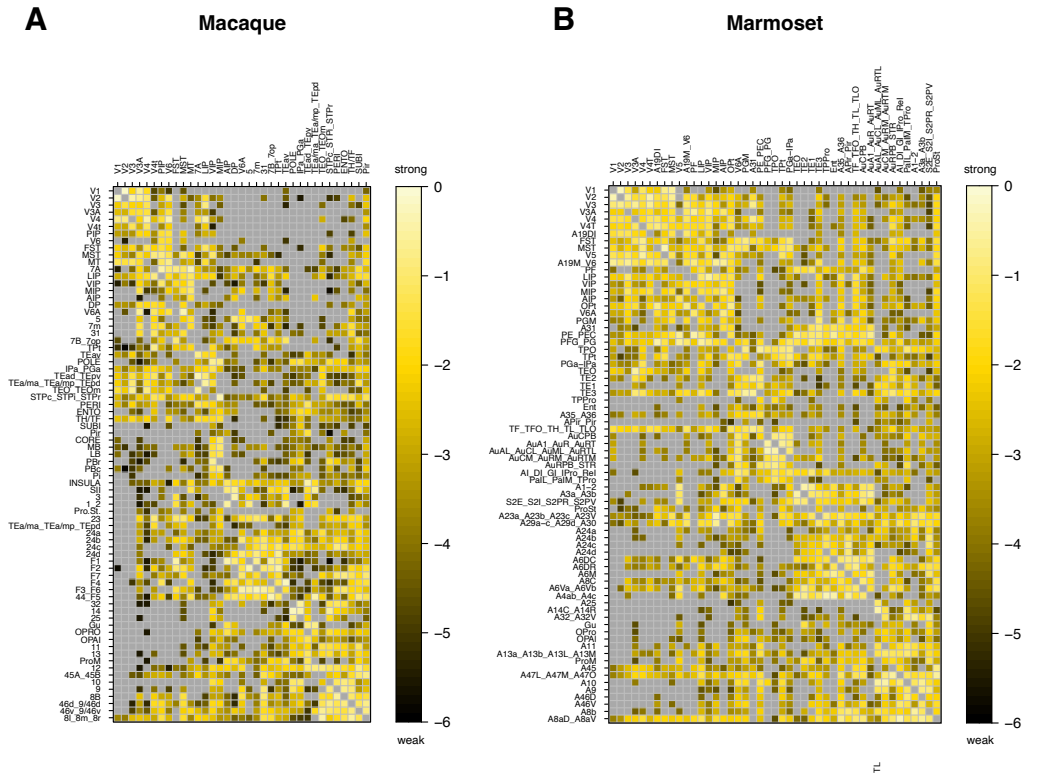

Figure S2: Full consensus FLN connectivity matrices. The consensus mapping reduces both species' atlases to a common parcellated of 74 areas, plus the subiculum ("SUBI") in the macaque. Reading convention as in **Figure 2**. **(A)** After consensus, the macaque goes from a 40×91 matrix to a 35×75 matrices. **(B)** Similarly, the marmoset goes from 55×116 to 45×74.

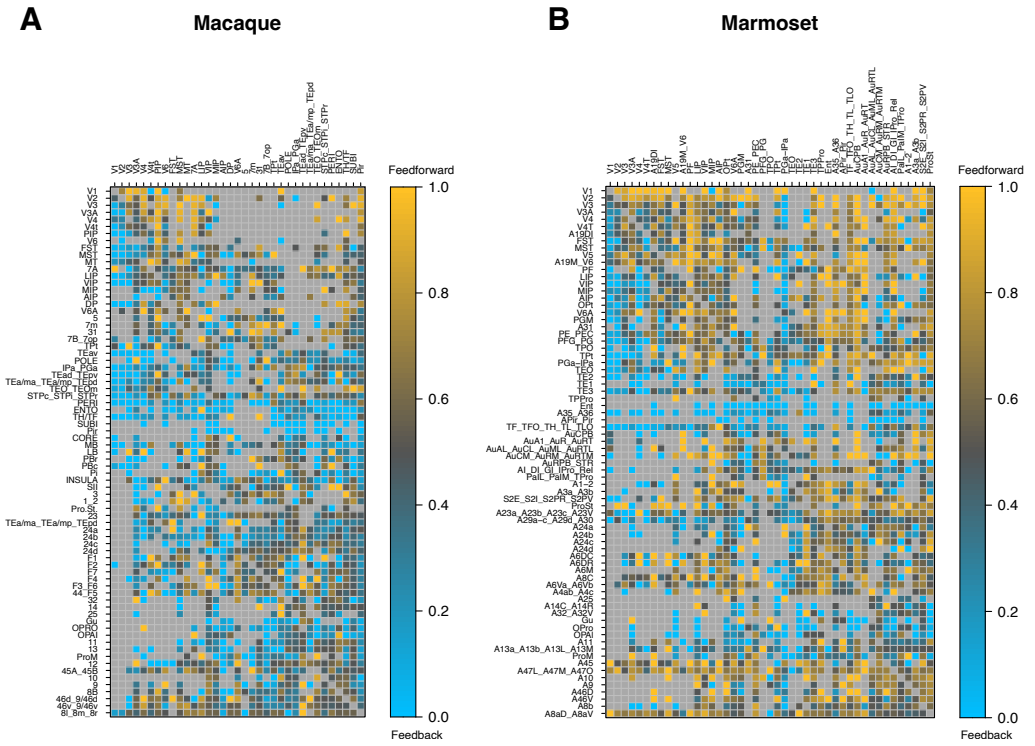

Figure S3: Full consensus SLN connectivity matrices. Same dimensions as in **Figure S2**. SLNs vary between 0 (FB; blue hues) and 1 (FF; yellow gold hues). **(A)** Macaque. **(B)** Marmoset.

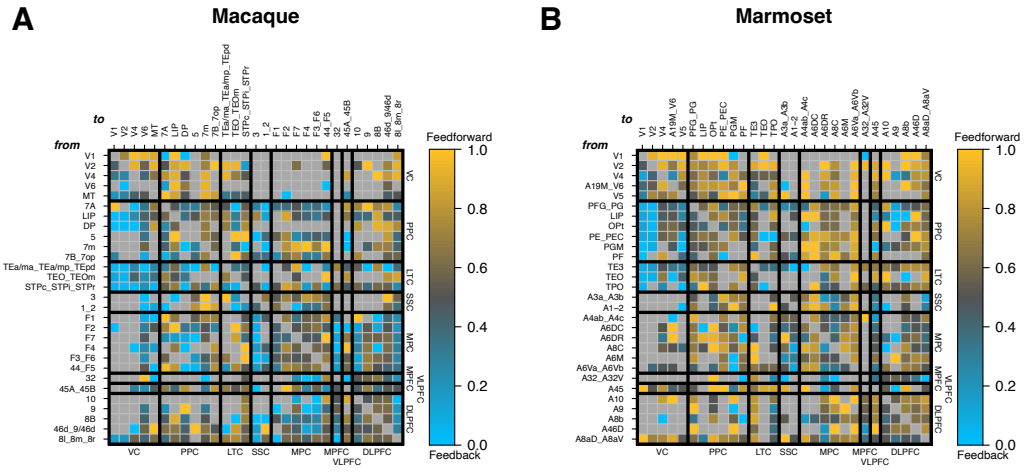

Figure S4: 29×29 common consensus SLN matrices for both species. All connections are here one-to-one comparable across species. Reading convention as in **Figure S3 (A)** Macaque. **(B)** Marmoset.

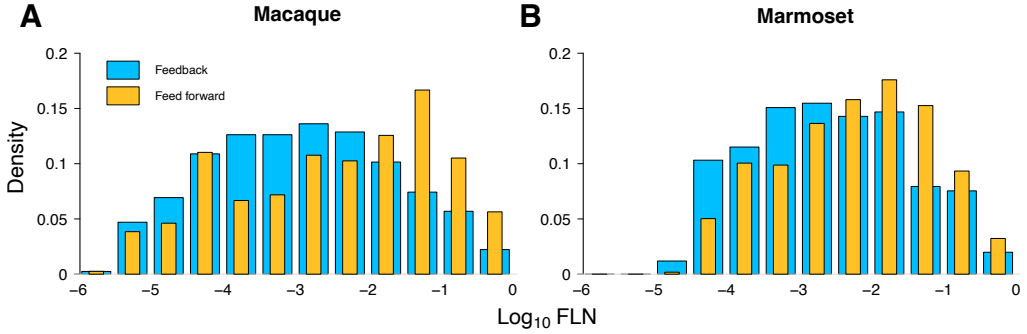

Figure S5: Feedback (FB) and feedforward (FW) distribution as a function of log_{10} FLN. Blue, feedback ; yellow, feedforward. **(A)** Macaque. **(B)** Marmoset.

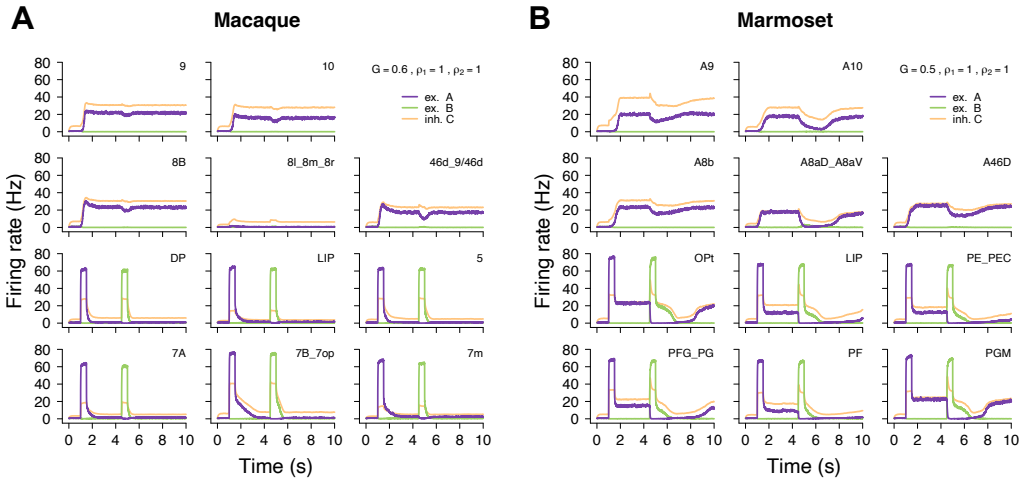

Figure S6: Alternative parametrization of global coupling parameter G. (A) Full example of firing rate as a function of time for the macaque's partially persistent regime at $G = 0.6$ from **Figure 5B**. **(B)** Full example behavior for the marmoset's small window of resilient regime at $G = 0.5$ from **Figure 5C**. Reading conventions as in **Figure 5B and C**.

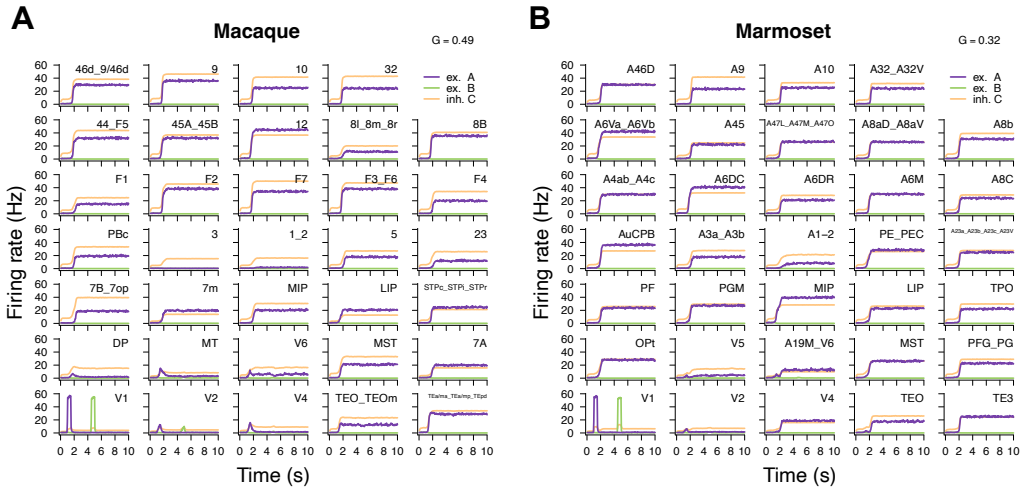

Figure S7: 29×29 area model of the distributed frontoparietal working memory model. (B) Marmoset. Global coupling parameter G, fixated at 0.49 for the macaque and 0.32 for the marmoset, was computed as in **Figure 5A**, over 8 different random seeds. Reading conventions as in **Figure 5B and C**. **(A)** Macaque.

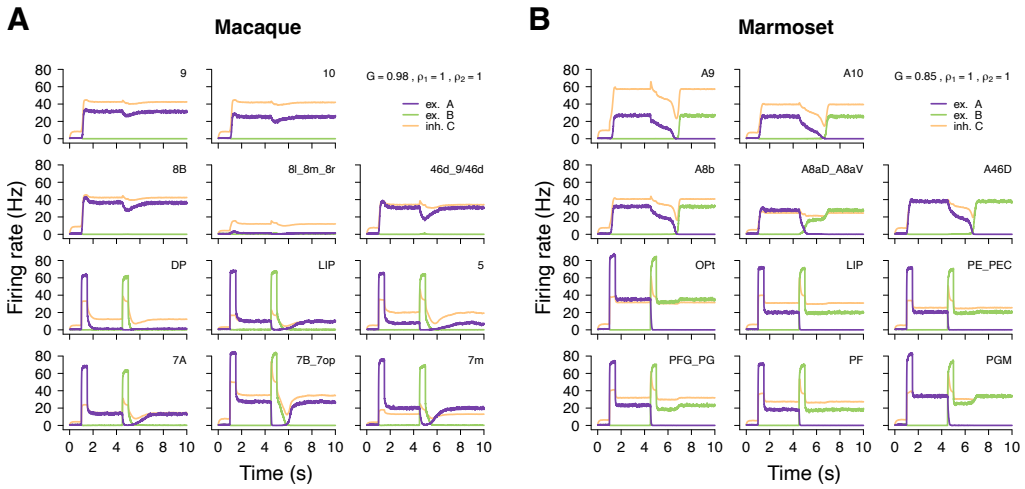

Figure S8: Model's behavior after swapping species specific connections. (A) The macaque connections (FLN and SLN) that do not exist in the marmoset were removed and replaced by the marmoset connections that do not exist in the macaque. Connections that exist in both were left unchanged. **(B)** Same procedure for the marmoset, performed in the opposite direction. G parameters unchanged. Reading conventions as in **Figure 5B and C**.

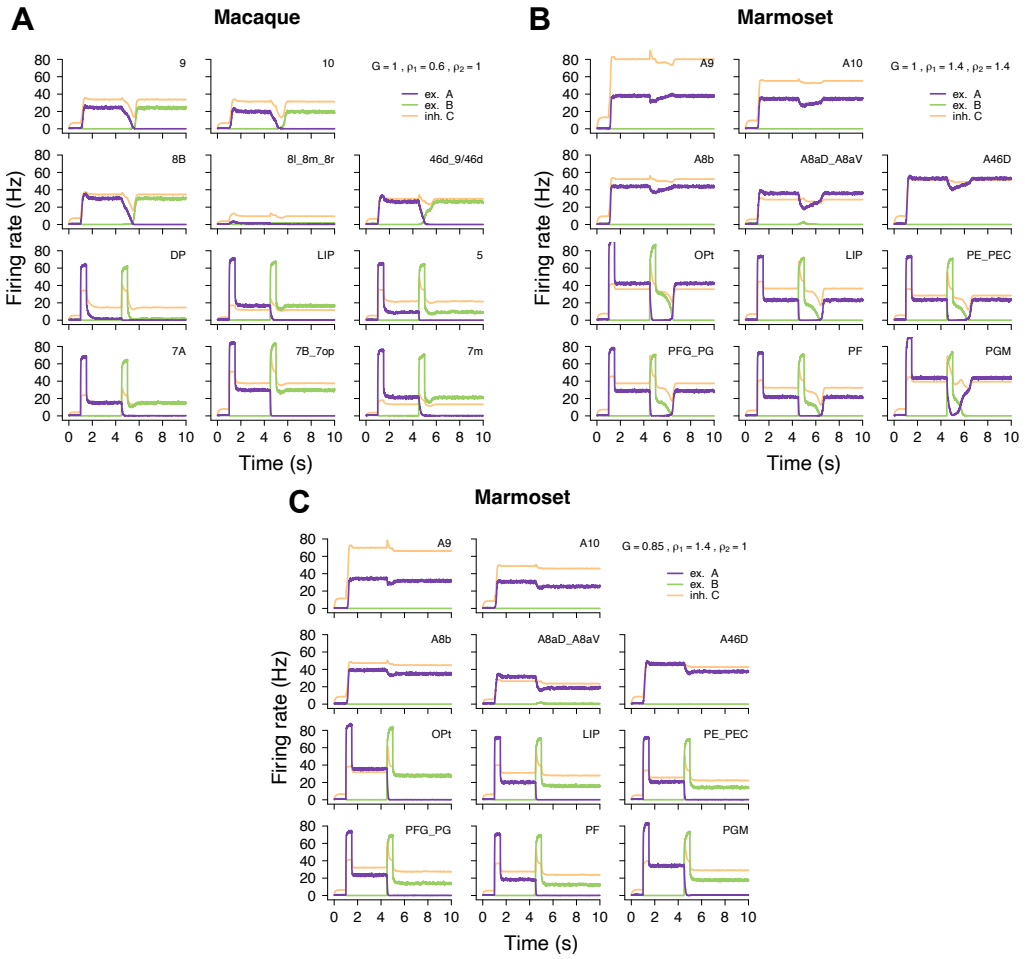

Figure S9: $\rho_1 - \rho_2$ Parameter space examples of resilience, distractibility and mixed behavior. **(A)** Full example behavior for the macaque's distractible regime at $G = 0.98,\ \rho_1 = 0.6,\ \rho_2 = 1$. **(B)** Full example behavior for the marmoset's resilient regime at $G = 0.85,\ \rho_1 = 1.4,\ \rho_2 = 1.4$. **(C)** Full example behavior for the marmoset's mixed regime at $G = 0.85,\ \rho_1 = 1.4,\ \rho_2 = 1$.

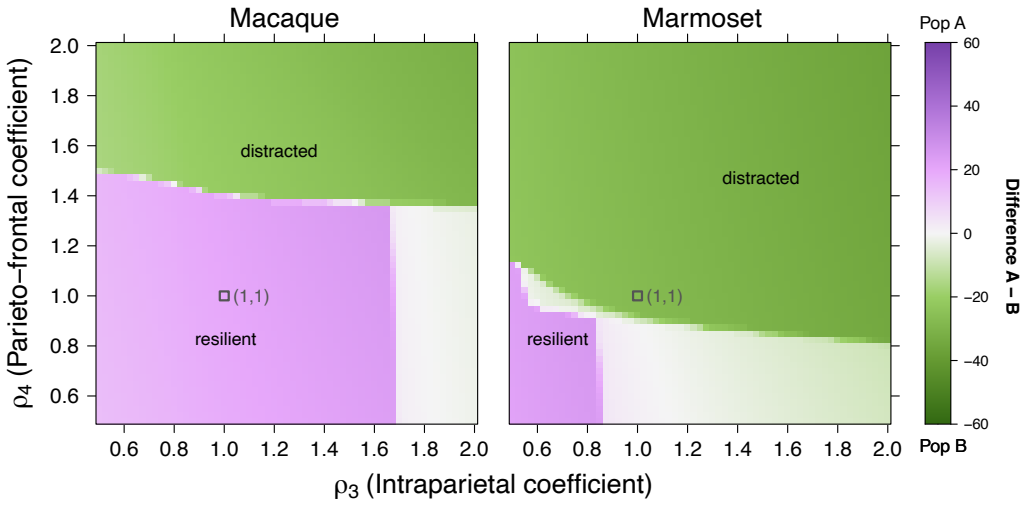

Figure S10: $\rho_3 - \rho_4$ Parameter space analysis of resilience and distractibility. Reading conventions as in **Figure 7B**). Each square is the average of simulations performed over 10 different random seeds, by incremental steps of 0.025 in both directions. Black open squares indicate (1,1) coordinates in the plane.

Consensus area	$\hat{h}$	Spine count	Source	Area name in source
V1	0	643 $\langle 688, 597 \rangle$	Elston et al. 1999 Elston and Rosa, 1997	V1
V2	0.132269	1201	Elston and Rosa, 1997	V2
V4	0.374088	2429	Elston and Rosa, 1998b	V4
3	0.377149	2987	Elston and Rockland 2002	3b
V6	0.488866			
1_2	0.552926			
DP	0.601343			
MT	0.613831	2077	Elston and Rosa 1997	MT
TEO_TEOm	0.641515	4800	Elston et al. 2010a	TEO
5	0.673251	4689	Elston and Rockland 2002	5
8l_8m_8r	0.68387	3200	Elston and Rosa, 1998a	FEF
F1	0.709641	4568	Elston and Rockland 2002	4
F4	0.735719			
F3_F6	0.792739	8238	Elston and Rockland 2002	6
32	0.800469			
10	0.825804	6488 $\langle 6887, 6090 \rangle$	Elston et al. 2011a	10
44_F5	0.843874	8238	Elston and Rockland 2002	6
7A	0.851916	2572	Elston and Rosa 1997	7a
45A_45B	0.858629			
46d_9/46d	0.858915	6584 $\langle 6621, 6548 \rangle$	Elston et al. 2011a	46
LIP	0.869096	2316	Elston and Rosa 1997	LIPv
7m	0.904036	2294	Elston 2001	7m
7B_7op	0.904156	6841	Elston and Rockland 2002	7b
F7	0.92325	8238	Elston and Rockland 2002	6
8B	0.923584			
STPc_STPi_STPr	0.924344	3585	Elston 2001	STPp
9	0.947519	7637	Elston et al. 2011a	9d
F2	0.981861	8238	Elston and Rockland 2002	6
TEa/ma_TEa/mp_TEpd	1	6730 $\langle 7260, 6200 \rangle$	Elston et al. 1999 (TEad) Elston et al. 2009 (TEpd)	TE

Table S1: Macaque spine count, hierarchical values and literary sources. $\hat{h}$ are the SLN based hierarchical position estimates. For V1, area 10, and consensus areas 46d_9/46d and TEa/ma_TEa/mp_TEpd, spine count values at the top are the mean of the values held between angular brackets just below. The last column indicates the name of the area for which the count was made in its original atlas conventions.

Consensus area	$\hat{h}$	Spine count	Source	Area name in source
V1	0	950	Oga et al. 2013	V1
V2	0.180824	1240	Elston et al. 1999	V2
V5	0.429611	2359	Elston et al. 1999	MT
A19M_V6	0.508004	1338	Elston et al. 1999	DM
A9	0.565519	4843	Sasaki et al. 2015	8B/9
A10	0.571427	3983	Elston et al. 2001	8B/9
TEO	0.593298	3465	Elston et al. 1999	TEO
A1-2	0.606556			
V4	0.643048	2098	Elston et al. 1999	DL
A45	0.645245			
A8aD_A8aV	0.691981			
PF	0.692536			
A6DR	0.693295			
LIP	0.709286			
A3a_A3b	0.723727			
A8C	0.732859			
PE_PEC	0.737931			
A46D	0.747617			
TE3	0.748794	3100	Oga et al. 2013	TE3
TPO	0.761058			
PFG_PG	0.768203			
PGM	0.777864			
A6M	0.791358			
OPt	0.805353			
A8b	0.809164	4843	Sasaki et al. 2015	8B/9
A4ab_A4c	0.819596			
A32_A32V	0.823476			
A6DC	0.93911			
A6Va_A6Vb	1			

Table S2: Marmoset spine count, hierarchical values and literary sources. Reading conventions as in **Table S1**.

Table S3: Consensus mapping atlas equivalence table. original atlases from Markov et al. (2014a) for the macaque and from Theodoni et al. (2022) for the marmoset.

Macaque	Marmoset	Region	Abbreviation
V1	V1	Visual Cortex	VC
V2	V2	Visual Cortex	VC
V3	V3	Visual Cortex	VC
V3A	V3A	Visual Cortex	VC
V4	V4	Visual Cortex	VC
V4t	V4T	Visual Cortex	VC
PIP	A19DI	Visual Cortex	VC
V6	A19M	Visual Cortex	VC
V6	V6	Visual Cortex	VC
FST	FST	Visual Cortex	VC
MST	MST	Visual Cortex	VC
MT	V5	Visual Cortex	VC
7op	PF	Posterior Parietal Cortex	PPC
7A	PFG	Posterior Parietal Cortex	PPC
7A	PG	Posterior Parietal Cortex	PPC
7B	PF	Posterior Parietal Cortex	PPC
LIP	LIP	Posterior Parietal Cortex	PPC
VIP	VIP	Posterior Parietal Cortex	PPC
MIP	MIP	Posterior Parietal Cortex	PPC
AIP	AIP	Posterior Parietal Cortex	PPC
DP	OPt	Posterior Parietal Cortex	PPC
V6A	V6A	Posterior Parietal Cortex	PPC
5	PE	Posterior Parietal Cortex	PPC
5	PEC	Posterior Parietal Cortex	PPC
7m	PGM	Posterior Parietal Cortex	PPC
31	A31	Posterior Parietal Cortex	PPC
STPr	TPO	Lateral Temporal Cortex	LTC
STPi	TPO	Lateral Temporal Cortex	LTC
STPc	TPO	Lateral Temporal Cortex	LTC
TPt	TPt	Lateral Temporal Cortex	LTC
PGa	PGa-IPa	Lateral Temporal Cortex	LTC
IPa	PGa-IPa	Lateral Temporal Cortex	LTC
TEO	TEO	Lateral Temporal Cortex	LTC
TEOm	TEO	Lateral Temporal Cortex	LTC
TEav	TE1	Lateral Temporal Cortex	LTC
TEpv	TE2	Lateral Temporal Cortex	LTC
TEad	TE2	Lateral Temporal Cortex	LTC
TEpd	TE3	Lateral Temporal Cortex	LTC
TEa/ma	TE3	Lateral Temporal Cortex	LTC
TEa/mp	TE3	Lateral Temporal Cortex	LTC
POLE	TPPro	Lateral Temporal Cortex	LTC

Continued on next page

Table S3– *Continued from previous page*

Macaque	Marmoset	Region	Abbreviation
PERI	A35	Ventral Temporal Cortex	VTC
PERI	A36	Ventral Temporal Cortex	VTC
ENTO	Ent	Ventral Temporal Cortex	VTC
TH/TF	TF	Ventral Temporal Cortex	VTC
TH/TF	TFO	Ventral Temporal Cortex	VTC
TH/TF	TH	Ventral Temporal Cortex	VTC
TH/TF	TL	Ventral Temporal Cortex	VTC
TH/TF	TLO	Ventral Temporal Cortex	VTC
Pir	APir	Ventral Temporal Cortex	VTC
Pir	Pir	Ventral Temporal Cortex	VTC
CORE	AuA1	Auditory Cortex	AUD
CORE	AuR	Auditory Cortex	AUD
CORE	AuRT	Auditory Cortex	AUD
MB	AuCM	Auditory Cortex	AUD
MB	AuRM	Auditory Cortex	AUD
MB	AuRTM	Auditory Cortex	AUD
LB	AuAL	Auditory Cortex	AUD
LB	AuCL	Auditory Cortex	AUD
LB	AuML	Auditory Cortex	AUD
LB	AuRTL	Auditory Cortex	AUD
PBr	AuRPB	Auditory Cortex	AUD
PBc	AuCPB	Auditory Cortex	AUD
Pi	PaIL	Insula	INS
Pi	PaIM	Insula	INS
Pi	TPro	Insula	INS
INSULA	AI	Insula	INS
INSULA	DI	Insula	INS
INSULA	GI	Insula	INS
INSULA	IPro	Insula	INS
INSULA	ReI	Insula	INS
SII	S2E	Somato Sensory Cortex	SSC
SII	S2I	Somato Sensory Cortex	SSC
SII	S2PR	Somato Sensory Cortex	SSC
SII	S2PV	Somato Sensory Cortex	SSC
1	A1-2	Somato Sensory Cortex	SSC
2	A1-2	Somato Sensory Cortex	SSC
3	A3a	Somato Sensory Cortex	SSC
3	A3b	Somato Sensory Cortex	SSC
Pro.St.	ProSt	Posterior Cingulate Cortex	PCC
23	A23a	Posterior Cingulate Cortex	PCC
23	A23b	Posterior Cingulate Cortex	PCC
23	A23c	Posterior Cingulate Cortex	PCC
23	A23V	Posterior Cingulate Cortex	PCC

Continued on next page

Table S3– *Continued from previous page*

Macaque	Marmoset	Region	Abbreviation
29/30	A29a-c	Posterior Cingulate Cortex	PCC
29/30	A29d	Posterior Cingulate Cortex	PCC
29/30	A30	Posterior Cingulate Cortex	PCC
24a	A24a	Anterior Cingulate Cortex	ACC
24b	A24b	Anterior Cingulate Cortex	ACC
24c	A24c	Anterior Cingulate Cortex	ACC
24d	A24d	Anterior Cingulate Cortex	ACC
F1	A4ab	Motor Premotor Cortex	MPC
F1	A4c	Motor Premotor Cortex	MPC
F2	A6DC	Motor Premotor Cortex	MPC
F7	A6DR	Motor Premotor Cortex	MPC
F3	A6M	Motor Premotor Cortex	MPC
F6	A6M	Motor Premotor Cortex	MPC
F4	A8C	Motor Premotor Cortex	MPC
F5	A6Va	Motor Premotor Cortex	MPC
F5	A6Vb	Motor Premotor Cortex	MPC
44	A6Va	Motor Premotor Cortex	MPC
44	A6Vb	Motor Premotor Cortex	MPC
32	A32	Medial PreFrontal Cortex	MPFC
32	A32V	Medial PreFrontal Cortex	MPFC
14	A14C	Medial PreFrontal Cortex	MPFC
14	A14R	Medial PreFrontal Cortex	MPFC
25	A25	Medial PreFrontal Cortex	MPFC
Gu	Gu	Orbital PreFrontal Cortex	OPFC
OPRO	OPro	Orbital PreFrontal Cortex	OPFC
OPAI	OPAl	Orbital PreFrontal Cortex	OPFC
11	A11	Orbital PreFrontal Cortex	OPFC
13	A13a	Orbital PreFrontal Cortex	OPFC
13	A13b	Orbital PreFrontal Cortex	OPFC
13	A13L	Orbital PreFrontal Cortex	OPFC
13	A13M	Orbital PreFrontal Cortex	OPFC
ProM	ProM	VentroLateral PreFrontal Cortex	VLPFC
45B	A45	VentroLateral PreFrontal Cortex	VLPFC
45A	A45	VentroLateral PreFrontal Cortex	VLPFC
12	A47L	VentroLateral PreFrontal Cortex	VLPFC
12	A47M	VentroLateral PreFrontal Cortex	VLPFC
12	A47O	VentroLateral PreFrontal Cortex	VLPFC
10	A10	DorsoLateral PreFrontal Cortex	DLPFC
9	A9	DorsoLateral PreFrontal Cortex	DLPFC
46d	A46D	DorsoLateral PreFrontal Cortex	DLPFC
46v	A46V	DorsoLateral PreFrontal Cortex	DLPFC
9/46d	A46D	DorsoLateral PreFrontal Cortex	DLPFC
9/46v	A46V	DorsoLateral PreFrontal Cortex	DLPFC

Continued on next page

Table S3– *Continued from previous page*

Macaque	**Marmoset**	**Region**	**Abbreviation**
8B	A8b	DorsoLateral PreFrontal Cortex	DLPFC
8l	A8aD	DorsoLateral PreFrontal Cortex	DLPFC
8l	A8aV	DorsoLateral PreFrontal Cortex	DLPFC
8m	A8aD	DorsoLateral PreFrontal Cortex	DLPFC
8m	A8aV	DorsoLateral PreFrontal Cortex	DLPFC
8r	A8aD	DorsoLateral PreFrontal Cortex	DLPFC
8r	A8aV	DorsoLateral PreFrontal Cortex	DLPFC

Parameter	Value	Explanation
	Current equation parameters	
J_c	0.0107	Cross-coupling current for E pop [nA]
J_{EI}	-0.31	Coupling current from I to E pop [nA]
J_{II}	-0.12	Coupling current from I to I pop [nA]
I_{0AB}	0.3294	Background current for E pop [nA]
I_{0C}	0.26	Background current for I pop [nA]
	Conductance equation parameters	
τ_N	0.06	NMDA excitatory time constant [s]
τ_G	0.005	GABA inhibitory time constant [s]
γ	1.282	Saturation factor for excitatory conductances [∅]
γ_I	2	Saturation factor for inhibitory conductance [∅]
	Noise equation parameters	
τ_n	0.002	Noise time constant [s]
σ_{AB}	0.01	Noise magnitude for excitatory pop A and B[nA]
σ_C	0	Noise magnitude for inhibitory pop C [nA]
	Transfer function Parameters	
a	135	Slope coefficient [Hz/nA]
b	54	intercept [Hz]
d	0.308	exponential coefficient [s]
g_I	4	Descaling parameter [∅]
c_0	177	Frequency threshold [Hz]
c_1	615	Conversion slope [Hz/nA]
r_0	5.5	intercept [Hz]
τ_r	0.002	Firing rate time constant [s]
	Synaptic strength parameters	
J_{min}	0.21	Minimal synaptic strength [nA]
J_{max}	0.42	Maximal synaptic strength [nA]
J_0	0.2112	Basic synaptic strength for computing gradient of J_{IE} [nA]
	Inter-areal connectivity	
G	0.98-0.85	Global coupling strength [∅]
k_1	1.2	FLN scaling parameter 1 [∅]
k_2	0.3	FLN scaling parameter 2 [∅]
ρ_1	1	FLN amplification from PFC to PFC [∅]
ρ_2	1	FLN amplification from PFC to PPC [∅]
ρ_3	1	FLN amplification from PPC to PPC [∅]
ρ_4	1	FLN amplification from PPC to PFC [∅]

Table S4: Marmoset pine count, hierarchical values and literary sources. Reading conventions as in **Table S1**. All parameter values are taken from Mejias and Wang (2022) apart from G and ρ.

Downloadable supplementary material

Videos S1 and S2

Table S5

Simulation code